POLYPUBLIE
Polytechnique Montréal

POLYTECHNIQUE MONTRÉAL
UNIVERSITÉ D'INGÉNIERIE

Titre: Title: Lattice Boltzmann Approach for the Modeling and Simulation of Water Droplets Impact and Freezing

Auteur: Author: Jesus Garcia Perez

Date: 2020

Type: Mémoire ou thèse / Dissertation or Thesis

Référence: Citation: Garcia Perez, J. (2020). Lattice Boltzmann Approach for the Modeling and Simulation of Water Droplets Impact and Freezing [Master's thesis, Polytechnique Montréal]. PolyPublie. https://publications.polymtl.ca/5365/

Document en libre accès dans PolyPublie
Open Access document in PolyPublie

URL de PolyPublie: PolyPublie URL: https://publications.polymtl.ca/5365/

Directeurs de recherche: Advisors: Jean-Yves Trépanier, Marcelo Reggio, & Sébastien Leclaire

Programme: Program: Génie aérospatial

Ce fichier a été téléchargé à partir de PolyPublie, le dépôt institutionnel de Polytechnique Montréal
This file has been downloaded from PolyPublie, the institutional repository of Polytechnique Montréal

https://publications.polymtl.ca

POLYTECHNIQUE MONTRÉAL
affiliée à l'Université de Montréal

Lattice Boltzmann Approach for the Modeling and Simulation of Water Droplets Impact and Freezing

JESÚS GARCÍA PÉREZ
Département de génie mécanique

Mémoire présenté en vue de l'obtention du diplôme de *Maîtrise ès sciences appliquées*
Génie aérospatial

Août 2020

© Jesús García Pérez, 2020.

POLYTECHNIQUE MONTRÉAL
affiliée à l'Université de Montréal

Ce mémoire intitulé :

Lattice Boltzmann Approach for the Modeling and Simulation of Water Droplets Impact and Freezing

présenté par **Jesús GARCÍA PÉREZ**
en vue de l'obtention du diplôme de *Maîtrise ès sciences appliquées*
a été dûment accepté par le jury d'examen constitué de :

David VIDAL, président
Jean-Yves TRÉPANIER, membre et directeur de recherche
Marcelo REGGIO, membre et codirecteur de recherche
Sébastien LECLAIRE, membre et codirecteur de recherche
Ali BENMEDDOUR, membre

DEDICATION

A mis padres, Juan y Salomé,
mi hermana Salomé y mi hermano Adrián,
por su amor incondicional y
apoyo en todas mis decisiones.

ACKNOWLEDGEMENTS

Foremost, I would like to express my deepest gratitude to my advisor Jean-Yves Trépanier for all the support he gave me and for letting me pursue my master's studies in Polytechnique. I am also grateful to my co-advisors Marcelo Reggio and Sébastien Leclaire. Particularly, Sébastien was instrumental for his valuable experience and suggestions. His continued support and extensive knowledge of the method and numerical simulation have really helped me.

Besides my advisors, I would like to extend my sincere thanks to Sami Ammar. I very much appreciate his helpful contributions and his invaluable insight into my research project. He also played a decisive role in my first experience of teaching.

I also had the great pleasure of working with Michel Ho. Thank you for the stimulating discussions, your unconditional help, and of course for always being there too as my friend.

I would like to acknowledge the National Research Council and particularly to Ali Benmeddour for their financial support and for giving me an insight into an actual application of this work.

Last but not least, I am indebted to my family and all my friends, particularly to Antonio Domínguez and Léa Dallemane for being my family in Montreal, making this experience unforgettable, and for always being there for me throughout every moment. Thank you to Maxence Gross, for unplugging me from daily routine.

RÉSUMÉ

L'impact et la congélation des gouttelettes d'eau constituent la base du givrage sur les drones. Ce processus transitoire impliquant un transfert de masse et de chaleur entraîne des effets de givrage indésirables. Afin de diminuer le danger des opérations, ce phénomène pourrait être réduit avec l'utilisation des revêtements "glaciophobes". Des informations détaillées sur un processus aussi complexe peuvent être obtenues à partir de la simulation numérique de la solidification à l'échelle des gouttes. Dans ce contexte, la méthode Lattice Boltzmann est apparue comme une alternative prometteuse pour la simulation d'écoulements polyphasiques et de matériaux à changement de phase.

Ce mémoire présente un modèle de Boltzmann sur réseau multi-phasique avec changement de phase pour étudier l'impact des gouttelettes sur une surface froide suivi de la solidification. Le modèle proposé combine un modèle de changement de phase thermique à un composant avec un modèle multi-phasique. Ces deux modèles sont vérifiés séparément. Le modèle pseudo-potentiel avec une équation d'état réelle est utilisé pour simuler des ratios de densité élevés. Le modèle thermique est basé sur l'enthalpie et permet la modélisation du changement de phase. Le couplage se fait par la méthode de frontières immergées qui traite l'interface solide-liquide.

Le modèle couplé sera utilisé pour effectuer une comparaison qualitative avec des résultats expérimentaux et de simulation pour la congélation des gouttelettes en équilibre sur une surface. Par la suite, l'effet de plusieurs paramètres sur le processus de congélation est analysé. Les résultats de la simulation révèlent que les surfaces hydrophobes permettent de retarder le processus de congélation en raison de la réduction de l'aire du contact avec la surface. De plus, une température plus froide de la plaque entraînera une réduction du temps de congélation total. En ce qui concerne l'impact et le gel des gouttelettes d'eau, l'augmentation de la vitesse d'impact entraînera une plus grande aire de contact avec la surface. Cela fournira une plus grande surface pour le transfert de chaleur et, par conséquent, la congélation des gouttelettes sera plus rapide. Dans le même cas, les surfaces hydrophiles offrent une congélation anticipée car l'étalement sur la surface est plus important. Enfin, pour démontrer l'adaptabilité du modèle, nous simulons l'impact et le gel des gouttelettes sur un profil aérodynamique.

ABSTRACT

Water droplets impacting and freezing represent the basis of ice accretion on airframe of unmanned aerial vehicles (UAVs). This transient process involving mass and heat transfer leads to undesired icing effects. To mitigate the hazard caused by this phenomenon, icephobic coatings can be used. Detailed information on such a complex process can be acquired from the numerical simulation that directly solves the solidification process at the droplet scale. In this context, the Lattice Boltzmann method has emerged as a promising approach for simulating multi-phase flows and phase change.

The present thesis presents a multi-phase Lattice Boltzmann model with phase change for studying droplet impact on a cold surface followed by a solidification process. The proposed model combines a thermal single-component phase change model with a multi-phase model. These two models are verified separately. The pseudo-potential model with a real equation of state is used to simulate large density ratios of multi-phase flows. The thermal model is based on the enthalpy and allows the phase change modeling. The coupling is made through the immersed moving boundary method that handles the solid-liquid interface.

The coupled model was used to perform a qualitative comparison with experimental and simulation results for a static droplet freezing. Subsequently, the effect of several parameters on the freezing process is analyzed. Simulation results have revealed that hydrophobic surfaces allow delaying the freezing process because of the reduced area in contact with the surface. Besides, a cooler temperature of the plate will result in a reduction of the total freezing time. Regarding the impact and freezing of water droplets, the augmentation of impact velocity leads to a larger contact area with the surface. This will provide a larger area for heat transfer and as a result, the freezing of the droplet will be faster. For the same case, hydrophilic surfaces provide anticipated freezing as the spreading on the surface is larger. Finally, to demonstrate the adaptability of the model, we simulated droplets impact and freezing on an airfoil.

TABLE OF CONTENTS

LIST OF TABLES

LIST OF FIGURES

LIST OF SYMBOLS AND ACRONYMS

c	lattice speed
$C_{p,l}$	liquid specific heat capacity
$C_{p,s}$	solid specific heat capacity
D	droplet diameter
$\mathbf{e}_i$	discretized velocity in the ith direction
$\mathbf{F}$	total force
$\mathbf{F}_i$	fluid-fluid interaction force
$\mathbf{F}_s$	fluid-solid interaction force
$\mathbf{F}_g$	gravitational force
Fo	Fourier number
f	particle distribution function
f^{eq}	equilibrium particle distribution function
f_l	liquid fraction
$\mathbf{g}$	gravity constant
G	fluid-fluid interaction strength
G_s	fluid-solid interaction strength
H	enthalpy
L_{ls}	latent heat
p	pressure
Pr	Prandtl number
Re	Reynolds number
Ste	Stefan number
T	temperature
$\mathbf{u}$	velocity
$\mathbf{x}$	position of the lattice
α	Thermal diffusivity
ν	kinematic viscosity
φ	effective mass
ρ	density
ρ_m	intermediate density
τ	relaxation time
θ	contact angle
ω_i	weighted coefficient

BB	Bounce-Back
BC	Boundary Condition
BE	Boltzmann Equation
BGK	Bhatnagar-Gross-Krook
CE	Chapman-Enskog
CFD	Computational Fluid Dynamics
C-S	Carnahan-Starling
DnQm	LBM stencil of n dimensions and m discrete velocities
EDM	Exact Difference Method
EOS	Equation of State
IBS	Immersed moving Boundary Scheme
IPS	Ice Protection System
LBM	Lattice Boltzmann Method
N-S	Navier-Stokes
PDF	Particle Distribution Function
P-R	Peng-Robinson
S-C	Shan-Chen
UAV	Unmanned Aerial Vehicle

LIST OF APPENDICES

CHAPTER 1 INTRODUCTION

Ice build-up on airframe surfaces and rotor/propeller blades presents a major hazard to safe and efficient operations of unmanned aerial vehicles (UAVs) in the harsh Canadian weather (i.e. cold and humid environments). Over time, substantial progress has been made to reduce airframe ice accretion by introducing ice protection systems, certification process, and pilot training. To mitigate icing risk for UAVs, novel ice protection systems (IPS) are required as conventional IPS developed for manned aircraft are not suitable for UAVs. One such novel IPS solutions that are being considered for UAVs is icephobic coatings; i.e. coatings with low affinity for ice.

In-flight airframe icing occurs when supercooled water droplets freeze on impact with any part of the external structure of UAVs or their rotors propellers during flight as shown in Fig. (1.1). When the drone structure has a temperature that is below 0°C, the moisture of the atmosphere might turn into ice as a consequence of the immediate or secondary contact. The ice accretion characteristics (size, shape, extent, roughness, and translucency) are related to the atmospheric environment parameters, the flight condition, the geometry of the airframe component being iced, and the time in icing conditions [6]. Any ice climatology must be associated with humid, cold, cloudy conditions.

Figure 1.1 Icing on a carbon fiber propeller. Courtesy of the National Research Council Canada, Aerodynamics Laboratory & Transport Canada, RPAS Task Force Engineering

Several multiphase and thermal phenomena are associated with icing process such as super-

cooled water droplet impacting with aircrafts surfaces, possible runoff of a film of water on the surface, forced convection because of airflow, phase changes as evaporation and solidification and reduction of refrigeration capacity due to low heat transfer coefficient and high-pressure drop. All of these drive finally to aerodynamic effects by increasing drag, decreasing lift, and causing control problems. For UAVs, some specific issues are encountered. There is a need for passive systems as there is not sufficient energy available. For that reason, the formulation of new coating materials with superior icephobic properties is a very active area of research.

The impact and freezing of water droplets are the basis of ice accretion. Thus, understanding this phenomenon under different conditions will allow researchers to develop more efficient anti-icing methods. Despite the simplicity of the concept, frost formation is a complicated transient process with simultaneous heat and mass transfer. It has been found that this phenomenon is divided into three stages: crystal growth, frost layer growth, and frost layer full growth [7]. Each period time and frost shape are found to strongly depend on the cold surface temperature and the vapor concentration difference between the mean stream and the cooling surface.

Several approaches have been widely used to predict ice accretion such as : flight tests, engineering methods, experimental simulations, and numerical methods. Experimental simulations and flight tests deliver the exact shape of ice accretion but are too expensive to be fully adopted. For this reason, numerical simulations are widely used as they are more economical and can deliver a good approximation of ice accretion. The available macroscopic codes are usually based on 4 modules: air flow-field solution, droplets collection efficiency calculation, boundary layer characteristic evaluation, and ice amount evaluation via a thermodynamic model. There are two approaches for the second one: The Lagrangian method and the Eulerian two-phase flow method [8]. The Eulerian approach considers the droplets as a pseudo fluid which interpenetrates with the air. The procedure for collection efficiency is achieved by solving the velocity and apparent density distribution of droplets. On the other hand, the droplet's trajectory obtained through the motion equation of droplets is used for collection efficiency in the Lagrangian method. Even though these numerical models can provide a good approximation of ice accretion, there is still a lack of knowledge of the microscopic process of ice formation and solidification due to the existing limited experimental equipment. For that reason, numerical simulations of multiphase flows also need to be carried out.
The numerical simulation of multi-component flows with phase change appeared in recent years as a challenge, because of the inherent difficulty to follow the various fluid interfaces.

In parallel, the Lattice Boltzmann Method (LBM) has grown as a simulation alternative and is now a promising digital approach for the simulation of complex geometry and multiphase flows. The success of the simulations based on the LBM is primarily due to its kinetic nature, allowing the simulation of a dynamic interface to the macroscopic scale and the possibility to include surface properties, like contact angle, through special terms.

The present work is organized as follows. Firstly, chapter 2 presents a brief and concise literature review that covers the basics of the studied phenomenon, some experimental works found in the literature, and the basis of droplet impact and freezing simulations with a final focus on Lattice Boltzmann methods.

Chapter 3 presents the basis of the LBM. The conceptual framework from statistical mechanics to fluid dynamics and the theoretical foundation of lattice Boltzmann methods are constructed. This chapter also includes a discussion covering the boundary conditions and two test cases to verify the ability of the lattice Boltzmann method to solve weakly compressible Navier-Stokes equations.

Chapter 4 discusses the simulation of multiphase flows using the LBM. The Shan-Chen pseudo-potential model is used to perform two different test cases which allow us to verify the model. The different ways of including the fluid-fluid interaction force are presented.

Chapter 5 covers the basis of the thermal lattice Boltzmann method to solve advection-diffusion equations. This baseline is used for introducing the phase change model in chapter 6. The recent total enthalpy method for phase change is presented. Stefan problems are simulated and verified with the analytical solution. Finally, the coupling between the fluid and thermal fields is presented. The verification is made with a phase change case with natural convection.

Using the concepts and models of the previous chapters, chapter 7 combines the pseudo-potential model and the total enthalpy model to simulate the impact and freezing of water droplets. Firstly, the interactions with the surface are described. Then, we depict the coupled method of the considered hypothesis and limitations. To validate the proposed model, we carried out a qualitative comparative for a three-dimensional implementation of a static water droplet freezing. Finally, we analyzed the influences of contact angle, Stefan number, droplet size under different conditions and surfaces. The main conclusions of this work are outlined in the final chapter.

CHAPTER 2 LITERATURE REVIEW

This chapter describes the literature review which begins by describing the physics of water droplet impact and freezing. The different stages observed and the different parameters of influence are outlined. The second part focuses on some of the experimental works found in previous literature and their findings. This is followed by the presentation of the current methods used for simulating multi-phase flows and phase change with computational fluid dynamics. The fourth part discusses the application of the Lattice Boltzmann models in this field. We present what has been done with their advantages and also the existing limitations. Finally, the last section summarizes the objectives of the present work.

2.1 Description of the phenomenon

The ice accretion is based on the impact of supercooled water droplets which freeze when in contact with any external surface of the aircraft by providing a nucleation point. As it has been mentioned in the introduction, frost formation can be divided into three stages: crystal growth, frost layer growth, and frost layer full growth [7]. All stages are influenced by the cold surface temperature and the vapor concentration difference between the cooling surface and the mean stream.

The first stage includes the solidification process which is the most important, as it will define the area of the frozen droplet which will be in contact with the aircraft surface and will lead to the consecutive frost layer formation.

The solidification process of impinging supercooled water droplets is a complicated transient problem that involves mass and heat transfer simultaneously. This process starts with supercooled water droplets in a metastable equilibrium present in clouds. Some of these droplets may suffer induced homogeneous nucleation because of the increased rate of evaporation cooling by the airflow at low and high humidity environments [9]. However, those which remain liquid may impact a surface. This first contact with a substrate is influenced by several parameters such as the impact velocity, the surface temperature, and also, the surface wettability.

When a water droplet impacts on a surface, the process can be divided into two phases: an initial spreading phase which finishes when the droplet reaches the maximum spreading

diameter and the inertial force dominates; and a receding phase influenced by the surface tension where after some cycles, the droplet achieves a stationary state [10]. The impact velocity will influence the initial maximum spreading diameter and the speed of the solidification. A low-temperature value of the surface will lead to increased viscosity of the liquid and it will also affect the speed of solidification. Finally, the surface wettability influences the spreading and the final equilibrium shape of the droplet, and, in consequence, the solidification time.

Regarding the solidification process, it can be divided into four stages: pre-cooling or supercooling, recalescence, freezing, and solid cooling [7]. The first stage refers to the fact that the droplet is in a supercooled state. Recalescence stage is an abrupt increase of temperature related to the release of latent heat from nucleation; it is an almost instantaneous phenomenon; at least at the time scale studied. After that, the growth of solid-phase starts governed by the heat transfer rate from the droplet to the frozen part. Finally and once all the droplet is frozen, solid cooling means the reduction of the solid droplet temperature down to a steady value near the cold plate temperature. The solidification time will also be influenced by the same parameters of impact.

2.2 Experimental investigations of droplet impact and freezing

So far, several experiments have been carried out to study the process of a supercooled droplet impinging on a plate. Li et al. [10] carried out an experimental study to identify the solidification mechanism of a single water droplet impacting on an aluminum surface. They found that solidification process does not influence the initial spreading process, but of longer receding phases the elimination was remarkable. Xu et al. [11] studied the effect of the impact velocity on the change of droplet size. Their results showed that higher impact velocities led to the increase of the maximum deformed diameter.

The surface wettability represents one of the key parameters in the solidification of a water droplet on a cold plate [12]. The wettability of a solid by a liquid is measured by the contact angle which is the angle between the surface of the liquid and the outline of the contact surface. A high contact angle indicates that the droplet has low wetting so the liquid will not spread very much onto the surface. On the other hand, a low contact angle indicates that the surface is high wetting, meaning that the water droplet spreads out more on the surface. Depending on the contact angle, a surface can be hydrophobic when its static contact angle is $\theta > 90°$ and hydrophilic when $\theta < 90°$. Superhydrophobic surfaces characterize contact angles higher than $150°$ as illustrated in Fig. (2.1).

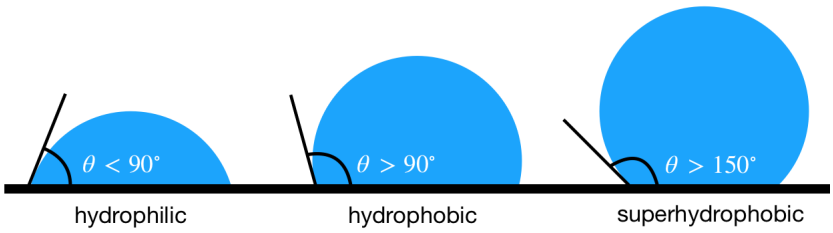

Figure 2.1 Behaviour of the material in function of contact angle

Huang et al. [13] studied the influence of the contact angle on the solidification process of a water droplet on a cold flat surface. They found that the freezing time of water droplets is strongly influenced by the contact angle: the larger the contact angle is, the longer the freezing time as the sphericity of the droplet increases, and the contact area between the droplet and the cold surface is smaller. This reduces the heat transfer from the cold surface and therefore the freezing process is slowed down. These results are supported by the works of Jin et al. [14] which found how the freezing time and the shape of the ice beads are affected by the different surfaces.

Jin et al. [15] studied the effects of the initial droplet height before impact and the cold plate temperature. For an increased initial height, the maximum spreading is increased while the height of the frozen droplet reduces significantly. Besides, for the same initial height, they found that a reduction of the ice surface temperature, the maximum spreading diameter, and the height of the ice bead is reduced. Their work provides practical information on droplet impact and freezing as a whole process, however, the evolution of the solidification front and the transient process is not explored.

2.3 Numerical simulation methods

The existing limited experimental methods and measurement techniques applied to these type of experiments prevent experimental results to provide detailed and accurate information about the process. As presented in the introduction, an experimental test of the ice accretion on a surface will provide the exact shape of the ice. However, apart from the high costs engaged, this test will not provide information about the freezing process of the water droplets impinging on a surface. Therefore, the related macroscopic codes in their Lagrangian or Eulerian version will not do it either. In the process of freezing of a water droplet on a cold plate, both the temperature distribution and phase transition processes are still not very clear. For this reason, the microscopic process is to be studied to predict

the phase transition process and temperature field. Numerical simulation is presented as an alternative to obtaining the data that experimental test simulations can not provide.

The simulation of a water droplet impact and freezing can be modeled with a multi-phase model that accounts for the presence of a liquid phase in a gas and allows interaction with the surface. On the other hand, it is intended to model the transient heat transfer during phase change, for which a thermal model is required [16]. Conventional computational fluid dynamics models that aim to solve multiphase flows are divided into two main categories [17]: Interface tracking methods and interface capturing methods. In the first one, a separate grid or a set of surface meshes is used to mark the location of the interface from an initial condition, and then it is explicitly calculated during the simulation. The arbitrary Lagrangian-Eulerian method, the boundary integral methods, and all front tracking methods belong to this category. In interface capturing methods, fluid properties change continuously across the interface from one fluid to another as the interface is represented by a function. The Volume of fluid (VOF) and phase field belong to this category. Some works on droplets spreading and freezing have been proposed with these methods.

Tabakoba et al. [18] developed an enthalpy based method solved numerically using the finite-difference technique to model the solidification process of a supercooled liquid droplet lying on a cold solid plate. They found that the total freezing time is increased by the thermal contact resistance of droplet with the wall.

Supercooled conditions on the impact and freezing of water droplets were investigated by Blake et al. [16]. A coupled VOF and level set method was used to capture the air-water interface, while the solid-liquid interface is captured with an enthalpy-porosity method. Their matching results allowed them to show the small influence of the supercooled state (first stage of solidification) on the simulation. However, the model presents some deficiencies as the change of density for solid state is not considered and the model is bidimensional.

A coupled volume of fluid (VOF) method and a dynamic contact angle model was recently presented by Tembely et al. [19]. Their model is based on the enthalpy formulation of energy equation to simulate water droplet impact, spreading and freezing under supercooled conditions. They found an exponential relation between the maximum spreading diameter and the total freezing time. As the solidification occurs during the kinematic phase the static contact angle is irrelevant and only the dynamic contact angle influences the spreading.

2.4 Lattice Boltzmann method

Alternatively, the lattice Boltzmann method has recently achieved success in some areas where traditional methods show difficulty performing the simulation of multiphase and multicomponent flows in complex geometries. This is due to its simplicity, local structure, ease in dealing with complex geometries, explicit nature, and suitability to use in distributed memory architectures.

There are several LB models proposed to solve multiphase flows: color gradient model [20], Shan-Chen pseudo-potential model [21], phase-field model [22] and free energy model [23] are frequently encountered. In the color-gradient model, two different distributions are used to represent two different fluids and an additional collision term is used for generating the surface tension. In the free energy model, two distribution functions are used. One is used to predict velocity but without considering the pressure gradient and the other one defines each phase as it calculates an order parameter. Finally, a Poisson-type equation is solved at each iteration step to find the exact velocity and pressure. The phase-field model solves the Cahn-Hilliard equation in addition to the Navier-Stokes equation to trace the interface between phases. The pseudo-potential model is probably the most frequently used as there is no need to add an equation to track the interface between phases and the interface is not introduced as a boundary condition. However, this model presents some problems like the presence of spurious currents and limitations of maximum density and viscosity ratio between phases. It also presents problems when using different viscosity fluids and thermodynamic consistency is not guaranteed. To solve the problem of coupling through viscosity, it is necessary to introduce a decoupling of surface tension and density.

Regarding the phase change, the LBM model for phase change has recently attracted great attention as it allows to track the liquid-solid interface automatically in a simple way. Many LBMs for solving the phase change have been proposed. They can be classified into three main methods [24]: enthalpy-based method, phase-field method, and the immersed boundary method. While the phase field and enthalpy methods allow to track the interface implicitly and are Eulerian methods, the immersed boundary-thermal lattice Boltzmann method tracks the interface explicitly by using a Lagrangian coordinate.

The phase-field method [25] introduces an auxiliary function that defines the solid and liquid fractions, by varying smoothly at the phase interface. The enthalpy based method [26] uses the evolution of the enthalpy to solve the temperature field and the phase interface is tracked

directly by the enthalpy formation. Finally, there is the immersed boundary-thermal LBM for solid-phase change proposed by Huang and Wu [27]. In this method, both velocity and temperature boundary conditions on the solid-liquid interface are solved by the immersed boundary method, and the interface is represented as a sharp interface rather than a diffusive interface. The pioneering work on phase change using the LBM has been carried out by Jiaung [26] in 2001. An iterative model to solve the LB equation without considering the convection term was presented and validated with Stefan problems.

All these multiphase and phase change LB models have proven that the LBM is a promising alternative over conventional methods and therefore a great tool for simulating multiphase flows and phase change materials. For such a reason, several LBM models of a water droplet impacting and/or freezing have been proposed in the literature for the integration of both models. They privileged the Shan-Chen pseudo-potential model to simulate multiphase/multicomponent flows, whereas enthalpy-based models are used for phase change.

Sun et al. [7] developed a LBM with phase change capabilities and applied it to the solidification of a static droplet on a surface. The iterative phase change model of Jiaung was coupled with the basic Shan-Chen model. Comparisons to their experimental data showed the potential of the approach. One of these authors added recently [28] a modification to their model, that takes into account the volume expansion of the droplet when freezing.

Xu et al. [29] proposed a more realistic two-dimensional model for the solidification of a water droplet on a substrate with the coupling between the multicomponent pseudo-potential model and the novel total enthalpy method for phase change. The interface treatment was made with the immersed boundary method. However, they did not present a comparison with other references or experimental results.

The aforementioned models simulated the solidification of static droplets on cold substrates. For water droplets impacting cold substrates and freezing, a model was proposed by Jianan et al. in 2017 [30]. They proposed a 2D coupled iterative's Jiaung phase change model with a multiphase S&C model improved by an equation of state. The interface treatment used was an immersed boundary scheme. The effects of the freezing temperature, impact velocity, and wettability on freezing time were investigated. Their results were not compared with other experimental or simulation results and only a cold spot was considered on the surface which is not very representative of the reality.

Subsequently, Xiong et al. [31] used a multicomponent pseudo-potential model coupled with Jiaung's iterative phase change model and the immersed boundary scheme to simulate a 3D droplet impact and freezing on a cold rough plate. The effects of the roughness of the substrate on the air entrapment for a droplet impact and solidification were studied.

2.5 Objectives

As we can infer, the LBM is a promising approach that has not been implemented yet deeply for the simulation of water droplet impact and freezing due to its recentness. However, its capabilities unveil an excellent potential to be explored. In this respect, this work has the following specific objectives to accomplish the main one, which is the LBM applied to the simulation of water droplet impact and freezing :

- Implement and verify a multiphase pseudo-potential model. This model will include a realistic equation of state to represent high-density ratios.
- Implement and verify the total enthalpy model for phase change which avoids iterations and allows to change thermal properties between liquid and solid.
- Integrate the verified models to simulate a water droplet impacting on a cold substrate followed by freezing.
- Achieve a 3D implementation.
- Validate the coupled model with experimental data and compare it to other references.

CHAPTER 3 LATTICE BOLTZMANN METHOD FOR WEAKLY COMPRESSIBLE NAVIER-STOKES EQUATIONS

3.1 Fundamentals of LBM

The flow simulation is performed by tackling a set of governing equations via numerical methods. Conventional computational fluid dynamics (CFD) addresses the problem by solving the Navier-Stokes (N-S) equations on a computational grid. This is a macroscopic modeling based on the continuum theory. In this context, standard numerical methods to carry out a flow simulation are finite differences, finite elements and finite volumes. At the other end of the flow simulation, we find the molecular dynamics approach. This is a microscopic view defined by modeling the movement and collision of individual molecules forming the fluid. The huge number of interactions, as well as their complexity, makes this alternative still unaffordable for practical purposes.

The Lattice Boltzmann Method (LBM) is a relatively recent model for simulating fluid flows. It does not use the continuum approach, neither the tracking of all individual molecules. Instead, it considers the behavior of an assemblage of molecules which moves on a lattice structure. According to this, the LBM establishes a link between micro and macro scales, and is therefore named a mesoscopic model. The simplified nature of the underlying kinetic model, allows this method for capturing macroscopic and mesoscopic physics, which leads to a better understanding of fluid flows. Figure 3.1 illustrates the three levels of modeling. From left to right: microscopic, mesoscopic and macroscopic. Regarding the microscopic scale on

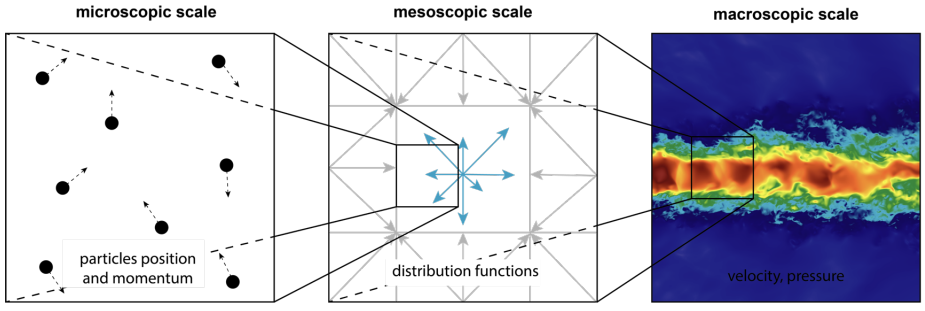

Figure 3.1 Different fluid scales

the left of Fig. (3.1), the motion of fluids made of a large number of molecular constituents obeys Newtonian mechanics. It is studied by the statistical physics dealing with the dy-

namics of non-equilibrium processes and their relaxation to the thermodynamic equilibrium: the kinetic theory (mesoscopic scale in the center of Fig. (3.1)). However, the resolution of systems made of a large number of degrees of freedom is troublesome. The fundamental idea of kinetic theory is to consider that the complete information for the statistical description of the fluid is contained in the single-particle distribution function (PDF), $f(\mathbf{r}, \xi, t)$, where $\mathbf{r}$ is the space coordinates, ξ is the microscopic velocity, t is the time. The symbol f represents the probability at the position $\mathbf{r}$ to possess a velocity ξ at the time t. At non-equilibrium statistic mechanics, the transport of the particles is described by the Boltzmann Equation [32] :

$$\frac{\partial f}{\partial t} + \mathbf{u} \cdot \nabla_{\mathbf{x}} f + \mathbf{a} \cdot \nabla_{\mathbf{v}} f = \Omega \tag{3.1}$$

The operators $\nabla_{\mathbf{x}}$ and $\nabla_{\mathbf{v}}$ are the gradient with respect to the spatial coordinates and the gradient in the velocity space, respectively. The velocity is represented by $\mathbf{u}$ and the acceleration by $\mathbf{a}$. The collision operator, Ω, is the term that accounts for the change of particle distribution due to collision. The Boltzmann equation is an integro-differential equation and the non-linear nature of the collision operator makes its solution an impossible task.
This induced difficulty of the collision term appeals for a model of simplification. The most commonly used and simple model is the Bhatnagar-Gross-Krook model (BGK) [33]. The BGK collision model approximates the change of distribution due to collision by a relaxation process towards the local equilibrium with a single relaxation time τ.

$$\frac{\partial f}{\partial t} + \mathbf{u} \cdot \nabla_{\mathbf{x}} f + \mathbf{a} \cdot \nabla_{\mathbf{v}} f = -\frac{f - f_{eq}}{\tau} \tag{3.2}$$

where f_{eq} defines the equilibrium distribution function which is given by the Maxwell-Boltzmann distribution depending on local hydrodynamic variables :

$$f_{eq} = n \left(\frac{m}{2\pi k_B T} \right)^{D/2} \exp\left(-\frac{m(\mathbf{v} - \mathbf{u})^2}{2k_B T} \right) \tag{3.3}$$

in which n, T, $\mathbf{u}$ are the macroscopic number density, temperature and velocity. The particle mass is given by m, D is the dimension of space and k_B is the Boltzmann constant.

This Boltzmann equation (BE), Eq. (3.1), with the BGK approximation of the collision term in Eq. (3.2), can therefore be discretized. For the sake of simplicity, the Boltzmann equation is considered without a force term, so $\mathbf{a} = 0$. The particle distribution function f is first discretized in the velocity space, where a set of discrete velocities $\mathbf{v}_i$ is used to replace the continuous spectrum of velocities. The BE is then defined in function of f_i, the function

distribution associated with $\mathbf{v}_i$ as follows :

$$\frac{\partial f_i}{\partial t} + \mathbf{v}_i \cdot \nabla_{\mathbf{x}} f_i = -\frac{f_i - f_i^{eq}}{\tau} \tag{3.4}$$

And then it can be discretized in space and time as follows :

$$f_i(\mathbf{x} + \mathbf{v}_i \delta t, t + \delta t) - f_i(\mathbf{x}, t) = -\frac{\delta t}{\tau}(f_i - f_i^{eq}) \tag{3.5}$$

The Eq. (3.5) is the base of the Lattice Boltzmann method (LBM) which can be seen as a two-step process: collision and advection (or streaming). When particles arrive at a grid point, the collision predicts the interaction between these particles and the change of their directions. This process is followed by the streaming where particles move to the neighbor grid points by following their velocity direction as illustrated in Fig. (3.2). The choice of the

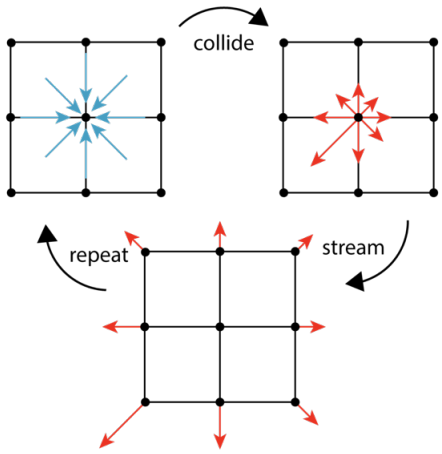

Figure 3.2 An overview of the collide-stream scheme of the LB algorithm

set of velocities determines the lattice structure. One of the most commonly used structure is the D2Q9 stencil, which has 9 lattice directions in 2 dimensional space. The dimensionless lattice speed is given by $c = \delta x/\delta t$ and the dimensionless lattice velocities $\bar{\mathbf{e}}_i = \mathbf{e}_i/c$ can be written as

$$\bar{\mathbf{e}}_i = \begin{cases} (0,0) & i = 0 \\ (\pm 1, 0), (0, \pm 1) & i = 1, 5, 3, 7 \\ (\pm 1, 1), (\pm 1, -1) & i = 2, 8, 4, 6 \end{cases} \tag{3.6}$$

By replacing the velocities $\mathbf{v}_i$ by $\mathbf{e}_i$, we get the working LBM equation :

$$f_i(\mathbf{x} + \mathbf{e}_i \delta t, t + \delta t) - f_i(\mathbf{x}, t) = -\frac{\delta t}{\tau}(f_i(\mathbf{x}, t) - f_i^{eq}(\mathbf{x}, t)) \tag{3.7}$$

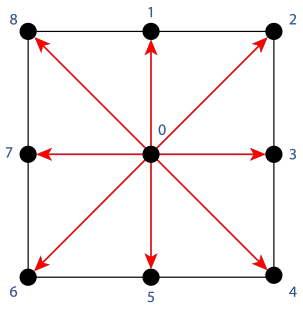

Figure 3.3 D2Q9 lattice swencil. The square denoted by black lines has an edge length $2\delta x$. Velocities are represented in red and rest velocity vector $\bar{\mathbf{e}}_0 = 0$ is not shown

The equilibrium distribution function is a truncated Maxwell-Boltzmann distribution function

$$f_i^{eq}(\rho, \mathbf{u}) = \rho\omega_i \left[1 + \frac{\mathbf{e}_i \cdot \mathbf{u}}{c_s^2} + \frac{\mathbf{uu} : (\mathbf{e}_i\mathbf{e}_i - c_s^2\mathbf{I})}{2c_s^2}\right] \tag{3.8}$$

where ω_i is the weighting factor for each lattice velocities. For D2Q9 these coefficients are

$$\omega_i = \begin{cases} 4/9 & i = 0 \\ 1/9 & i = 1, 3, 5, 7 \\ 1/36 & i = 2, 4, 6, 8 \end{cases} \tag{3.9}$$

The speed of sound in LBM is given by c_s. This value depends on the lattice structure as it is defined by $c_s = \frac{1}{\sqrt{3}}c$ for the most common one.

The relaxation time can be related to the fluid kinetic viscosity ν using a Chapman-Enskog expansion (CE). The CE is a multiscaling expansion technique for correlating the Boltzmann equation in kinetic theory under low Mach number assumption with a Navier-Stokes-like equation. This relationship is given by the following expression [34]:

$$\nu = \delta_t c_s^2 \left(\tau - \frac{1}{2}\right) \tag{3.10}$$

Finally, the macroscopic hydrodynamic quantities can be recovered from the summation of the discrete particle distribution functions. Density and flow velocity are obtained by the following equations

$$\rho = \sum_i f_i \tag{3.11}$$

$$\mathbf{v} = \frac{1}{\rho}\sum_i \mathbf{e}_i f_i \tag{3.12}$$

The algorithm of the LBM can be summarized as follows :

1. Initialize of distribution functions f_i respecting the initial and boundary conditions
2. Compute macroscopic variables : ρ, $\mathbf{v}$
3. Collision step
4. Streaming step
5. Apply boundary conditions
6. Repeat 2-5

3.2 Boundary conditions

In the LBM, the evolution of the fluid is determined by the distribution functions. Thus, the application of the hydrodynamics quantities on boundaries needs a translation of these macroscopic values to PDF. These discrete distribution functions have to be taken care of to reflect the macroscopic BCs of the fluid as they are critical to the stability and accuracy of any numerical solution. In this research, we explore three of the most widely used BCs: periodic, Bounce-Back, and Zou-He velocity BCs.

3.2.1 Periodic boundary conditions

Periodic boundary conditions represent the simplest boundary condition in LBM, which only requires copying the distribution functions from the opposite boundary. Fig. (3.4) shows the east-west periodic boundary conditions in which the unknown incoming populations on one side are given by those leaving the domain at the opposite side [32].

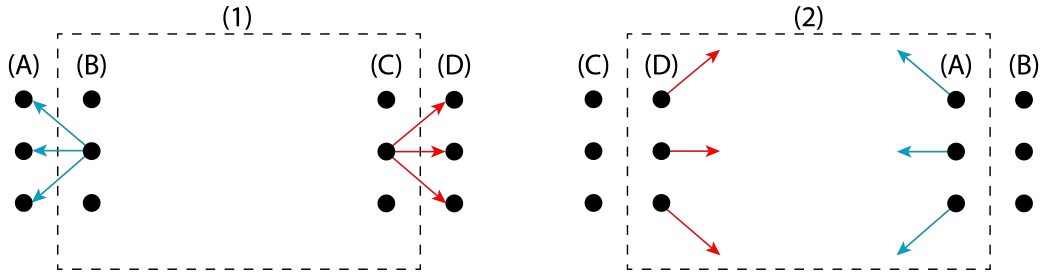

Figure 3.4 Periodic boundary conditions steps: (1) pre-streaming; (2) post-streaming.

3.2.2 Bounce-Back boundary conditions

Bounce-Back boundary conditions are typically used to implement no-slip conditions on the boundary. By the so-called bounce-back we mean that when a fluid particle reaches a boundary node, the particle will scatter back to fluid along with its incoming direction. Bounce-backs BCs come in a few variants and we will present two types of implementations: half-way bounce-back and full-way bounce-back. For both boundary conditions, the boundary is located approximately midway between solid and boundary nodes. The half-way bounce-back is particularly simple and preserves an acceptable numerical accuracy. A boolean mask can be used for the boundary and the interior nodes. The incoming directions of the distribution functions are reversed when coming across a boundary node. Considering a node immediately close to the boundary, the inversion process of the distribution function takes place during the streaming at the same time step t as illustrated in Fig. (3.5).

On the other hand, the full-way bounce-back BC requires solid nodes to store the distributions functions and then bounced back in the following collision step. This implementation is ideal when simulating fluid flows in complex geometries as it does not distinguish the orientation of the boundaries. At a given time step t, the distribution functions with directions towards the outside of the domain would leave the latter. The collision is then applied and directions of these distribution functions are reversed and they bounce back to the boundary nodes. The distribution functions at the end of bounce-back in this configuration are the post-collision distribution functions, the process ends at a time $t + 2\delta t$ in the propagation step as shown in Fig. (3.6).

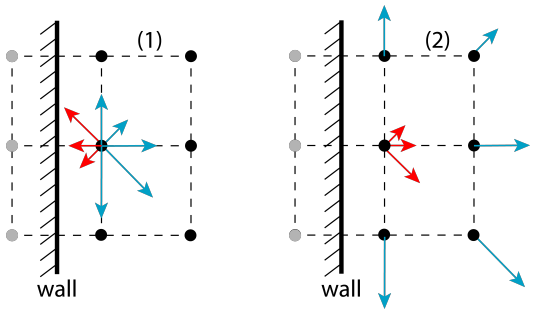

Figure 3.5 Half-way bounce-back boundary condition steps: (1) pre-streaming; (2) post-streaming

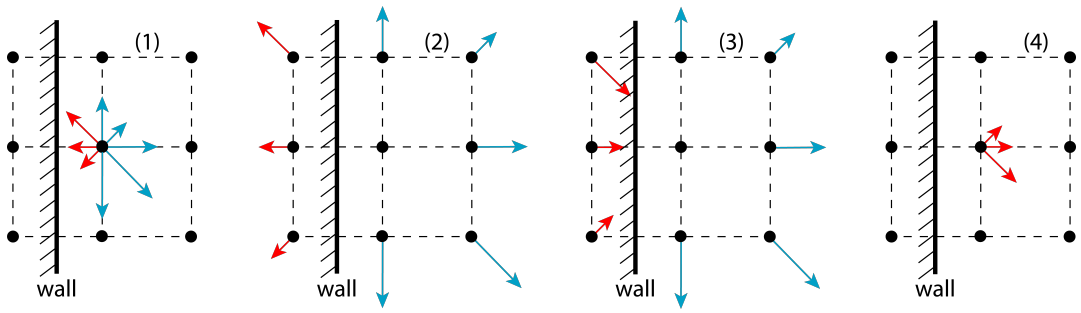

Figure 3.6 Full-way bounce-back boundary condition steps: (1) pre-streaming; (2) post-streaming; (3) post-collision; (4) post-streaming. The collision between (2) and (3) is only applied on fluid nodes

3.2.3 Zou-He velocity and pressure BCs

These BCs were originally developed by Zou and He [35] and allow us to model fluid flows with prescribed velocity or pressure (density) at the boundary. The idea behind Zou-He BCs is to formulate a linear system of the unknown distribution functions at the boundary and velocity (for a prescribed pressure) or density (for a prescribed velocity). To illustrate the method, we consider an imposed velocity $\mathbf{u}_N = [u, v]$ at the north boundary. After the streaming process, the distribution functions towards the fluid (f_4, f_5, f_6) and density ρ are unknown. Using the definition of the macroscopic moments in function of the PDF, we have :

$$\rho = f_0 + f_1 + f_2 + f_3 + f_4 + f_5 + f_6 + f_7 + f_8 \tag{3.13}$$

$$\rho u = f_3 - f_7 + f_2 - f_6 + f_4 - f_8 \tag{3.14}$$

$$\rho v = f_1 - f_5 + f_8 - f_6 + f_2 - f_4 \tag{3.15}$$

This gives three equations, so to close the system we need an additional equation. Following [35], the assumption for the remaining equation is that the bounce-back rule still holds for the non-equilibrium part of the particle distribution normal to the boundary. In that case, we have :

$$f_1 - f_1^{eq} = f_5 - f_5^{eq} \tag{3.16}$$

By solving the created system of four equations, we have :

$$\rho = \frac{f_0 + f_3 + f_7 + 2(f_1 + f_2 + f_8)}{1 + v} \tag{3.17}$$

$$f_5 = f_1 - \frac{2}{3}\rho v \tag{3.18}$$

$$f_4 = f_8 + \frac{\rho u}{2} + \frac{\rho v}{6} + \frac{f_7 - f_3}{2} \tag{3.19}$$

$$f_6 = f_2 - \frac{\rho u}{2} + \frac{\rho v}{6} + \frac{f_3 - f_7}{2} \tag{3.20}$$

Same procedure can be applied for other boundaries. In the case where pressure (or density) is specified at boundary, a similar procedure is performed but one of the velocity components must be provided for a two dimensional case.

3.3 Verification tests

The ability of the LBM to simulate fluid flows will be presented with the simulation of two simple benchmark tests: the Poiseuille flow and the lid-driven cavity flow. The simulation parameters and results compared with the analytical or numerical solution are presented for each case.

3.3.1 Poiseuille flow

The Poiseuille flow is defined as a steady, laminar flow between two horizontal parallel plates separated by a distance h. Both plates are considered to be at rest and flow is caused by a pressure gradient $\partial p/\partial x$ in the direction x parallel to the plates. Assuming that the only non-zero component of the velocity is u_x and that pressure and velocity are independent of time, the resulting continuity equation for an incompressible fluid yields :

$$\frac{\partial u_x}{\partial x} = 0 \tag{3.21}$$

so the component of velocity parallel to the plates, $u_x(y)$, is only a function of the coordinate perpendicular to the plates, y. For this case, the Navier-Stokes equations reduce to a second order, linear differential equation for an incompressible fluid of constant and uniform viscosity :

$$\frac{\partial p}{\partial x} = \mu \frac{\partial^2 u_x}{\partial y^2} \tag{3.22}$$

$$\frac{\partial p}{\partial y} = 0 \tag{3.23}$$

where μ and p are correspondingly the fluid dynamic viscosity and pressure. Furthermore, it is assumed that gravitational forces are negligible and the pressure gradient is constant. The integration of these equations with the application of non-slip conditions at the upper

and low plates yields :

$$u_x(y) = \frac{1}{2\mu}\left(-\frac{\partial p}{\partial x}\right) y(h-y) \tag{3.24}$$

As the fluid is considered to be incompressible and the kinetic theory links the fluid compressiblity to the definition of pressure, the pressure gradient must be sufficiently weak to consider that the fluid density is constant locally. The compressibility of a fluid is measured by the Mach number :

$$\mathrm{Ma} = \frac{u}{c_s} \tag{3.25}$$

The incompressible approximation is roughly verified when $\mathrm{Ma} < 0.1$, but compressibility error may remain if the Ma number is not decreased as the grid is refined [36].

The analytical and numerical solutions for the x-velocity are shown in Fig. (3.7). The developed LBM code is used to compute the flow on a 500×50 lattice arrangement. Figure 3.7 shows the steady-state streamwise velocity profile along a vertical line passing through the centre of the channel and the comparison of the velocity profile with the analytical solution. It is seen that the present LBM results agree well with the analytical results.

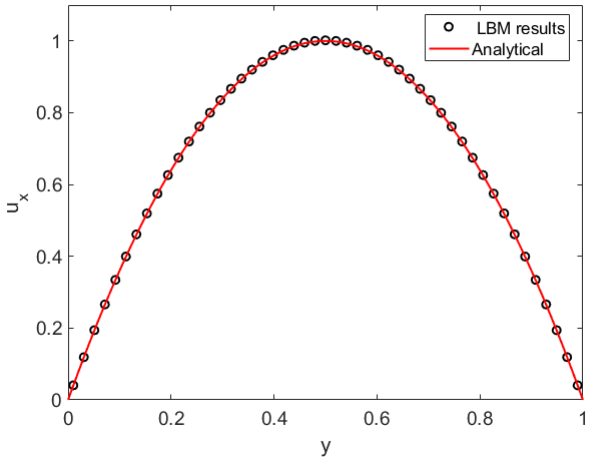

Figure 3.7 Streamwise velocity profile comparison between LBM simulation and analytical solution

3.3.2 Lid-driven Square cavity flow

For this test, a laminar flow inside a square cavity of which a lid moves at a constant velocity is considered. The model, based on the Navier-Stokes equations for solving this classical problem applies a non-slip velocity boundary condition to all the sides of the square domain

except for the lid where a constant velocity is fixed. For this type of geometry, the Reynolds number is based on the length of the moving lid, its speed, the fluid's viscosity and density following the expression :

$$\mathrm{Re} = \frac{\rho u_{max} L}{\mu} \tag{3.26}$$

In this test, we consider flows at different Reynolds numbers (Re = 100, 400). A grid of 200×200 lattices was used to perform these simulations. Fig. (3.8a) shows the total velocity profile for Re = 100. There is a central vortex and, even if not visible in this figure, recirculation areas at the bottom corners are also present. Their size and location vary according to the Reynolds number of the flow. Once a steady state is achieved, the velocity profiles are compared with those of Ghia et al. [1] who used a multigrid solution method for the N-S equations to simulate the lid-driven cavity. The results for the two considered Reynolds numbers are shown in Fig. (3.8). Comparisons show a good agreement with the reference which allows the ability of the LBM code to simulate incompressible flows.

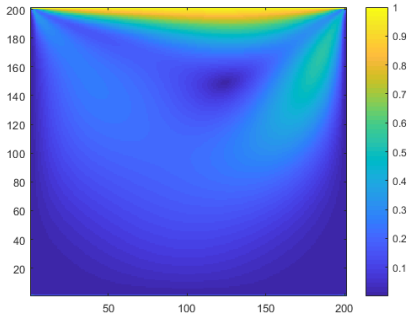

(a)

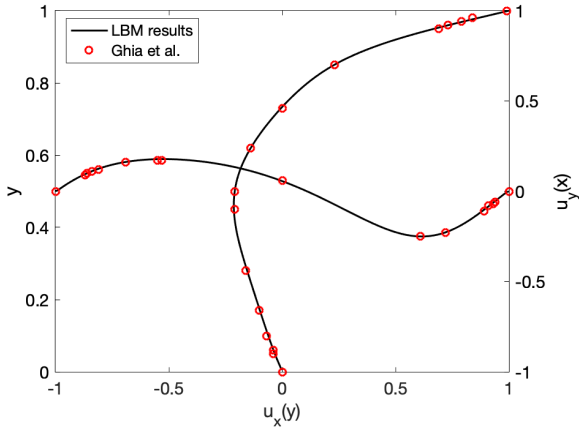

(b)

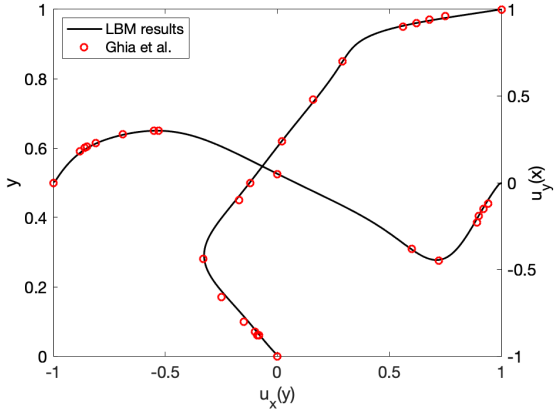

(c)

Figure 3.8 (a) Total velocity profile at Re = 100. Comparisons of LBM results with those of Ghia et al. [1] for (b) Re = 100 and (c) Re = 400

CHAPTER 4 MULTI-PHASE MODEL

4.1 Introduction

The simulation of a water droplet impacting on a flat surface must be accomplished by a multiphase model of the flow to consider both phases : liquid and vapour. As discussed before, there are several popular multiphase LBM models. However, for the present work, the chosen model to perform the simulations is the Shan & Chen pseudo-potential model.

This model was initially presented in 1993 by Shan & Chen (S-C) [21] to simulate multi-component and multi-phase flows with LBM. It uses an interparticle potential to mimic the interactions among the particles on the nearest and next-nearest neighbor sites.

The S-C model has the ability to track and separate the interface automatically, shows high computational efficiency and allows to model complex multiphase flows. However, the original S-C model cannot model flows with high viscosity and density ratios and an increased density ratio involves an increase of spurious currents which represent the variation of velocity from the real physical situation [37] and drives to numerical instabilities [38]. Additionally, it presents problems when using different viscosities as thermodynamic consistency is not guaranteed. In this section, we will use a modification of the original model to simulate larger density ratios and increase stability.

4.2 Fluid-fluid interaction

Shan & Chen model uses a pseudo-potential that depends on the local density to represent the microscopic interactions at the mesoscopic scale considering that the segregation of different phases is due to the long-range interaction between particles at site $\mathbf{x}$ and the particles at nearest and next-nearest neighbor sites $\mathbf{x}'$. Thus, if the intensity of the interaction is below a critical value, automatic phase separation occurs resulting in a low density phase and a high density phase. The interaction force between fluids is expressed as follows :

$$\mathbf{F} = -\varphi(\mathbf{x}) \sum_{\mathbf{x}'} G(\mathbf{x}, \mathbf{x}')\varphi(\mathbf{x}')(\mathbf{x}' - \mathbf{x}) \tag{4.1}$$

where φ is the effective mass function and depends on the local density. The Green's function $G(\mathbf{x}, \mathbf{x}')$ represents the intensity of the interparticle interaction of the nearest and next-nearest

sites and it is given by :

$$G(\mathbf{x},\mathbf{x}') = \begin{cases} G & |\mathbf{x}-\mathbf{x}'| = \delta x \\ G/4 & |\mathbf{x}-\mathbf{x}'| = \sqrt{2}\delta x \\ 0 & \text{otherwise} \end{cases} \tag{4.2}$$

G controls the strength of the interaction force and its sign determines if the force is attractive (negative) or repulsive (positive).

Most references present this interaction force as shown in Eq. (4.1) with a sum for all neighbor sites. However, it is an equivalent form for the discrete gradient of the effective mass :

$$\mathbf{F} = -c_0\varphi(\mathbf{x})g\nabla\varphi(\mathbf{x}) \tag{4.3}$$

where $g = G/2$ and c_0 is a constant that depends on the lattice structure. For D2Q9 stencil scheme, $c_0 = 6$. The developed gradient calculation for the two directions can be approximated by a linear weighted combination of the values $\varphi(c_x, c_y)$ (Fig. 4.1) as in Ref. [39] :

$$\nabla\varphi(\mathbf{x}) = \begin{bmatrix} \varphi_x \\ \varphi_y \end{bmatrix} = \frac{1}{3}\begin{bmatrix} \varphi_{i+1,j} - \varphi_{i-1,j} + \frac{1}{4}\left(\varphi_{i+1,j+1} - \varphi_{i-1,j+1} + \varphi_{i+1,j-1} - \varphi_{i-1,j-1}\right) \\ \\ \varphi_{i,j+1} - \varphi_{i,j-1} + \frac{1}{4}\left(\varphi_{i+1,j+1} - \varphi_{i+1,j-1} + \varphi_{i-1,j+1} - \varphi_{i-1,j-1}\right) \end{bmatrix} \tag{4.4}$$

The force is finally calculated using Eq. (4.3) as shown in Eq. (4.5)

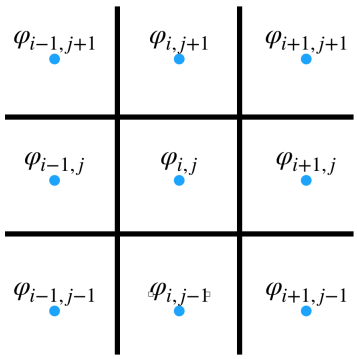

Figure 4.1 Detail of values used for the linear approximation of gradient

$$\mathbf{F} = \begin{bmatrix} F_x \\ F_y \end{bmatrix} = \begin{bmatrix} -\frac{2}{3}\varphi_{i,j} g[\varphi_{i+1,j} - \varphi_{i-1,j} + \frac{1}{4}(\varphi_{i+1,j+1} - \varphi_{i-1,j+1} + \varphi_{i+1,j-1} - \varphi_{i-1,j-1})] \\ \\ -\frac{2}{3}\varphi_{i,j} g[\varphi_{i,j+1} - \varphi_{i,j-1} + \frac{1}{4}(\varphi_{i+1,j+1} - \varphi_{i+1,j-1} + \varphi_{i-1,j+1} - \varphi_{i-1,j-1})] \end{bmatrix} \quad (4.5)$$

4.3 Effective mass

The effective mass is a function of the local density $\varphi(\mathbf{x}) = \varphi(\rho(\mathbf{x}))$ and its choice allows to simulate different fluid behaviors. Shan and Chen's original effective mass is given by $\varphi(\rho) = \rho_0 [1 - exp(-\rho/\rho_0)]$ where ρ_0 is a constant. However, this potential presents difficulties when simulating high density ratios.

This model is improved by introducing a more sophisticated equation of state (EOS). Considering that the ideal EOS of the system, $p = \rho c_s^2$, is corrected by the introduction of this interaction force, the following non-ideal EOS is given by :

$$p = c_s^2 \rho + \frac{c_0}{2} g[\varphi(\rho)]^2$$

A new effective mass can be defined as follows [21]:

$$\varphi(\rho) = \sqrt{\frac{2(p - c_s^2 \rho)}{c_0 g}}$$

the relationship between pressure and density depends on the choice of the EOS. It should be noted that with this definition of the effective mass and unlike the original Shan Chen model, the coefficient which models the interaction strength g, loses influence on the interaction force and the only condition required is to ensure that the whole term inside the square root is positive.

The choice of the EOS will determine the maximum density ratio and the influence of spurious currents. In this work, two cubic EOS are used and compared: Peng-Robinson (P-R) and Carnahan-Starling (C-S).

The P-R EOS is expressed as [40] :

$$p = \frac{\rho R T}{1 - bp} - \frac{a\alpha(T)\rho^2}{1 + 2b\rho - b^2\rho^2} \quad (4.6)$$

$$\alpha(T) = [1 + (0.37464 + 1.5422\omega - 0.26992\omega^2)(1 - \sqrt{T/T_c})]^2$$

with

$$a = \frac{0.45724 R^2 T_c^2}{p_c}$$

$$b = \frac{0.0778RT_c}{p_c}$$

where T is the absolute temperature of the fluid, a is the attraction parameter and b is the repulsion parameter; these parameters govern the surface tension. The critical temperature and critical pressure are given by T_c and p_c, respectively. The gas constant is R (set to $R = 1$ for all the simulations) and ω is the acentric factor ($\omega = 0.344$ for water [41]) which is a parameter that measures the non-sphericity of molecules.

For Carnahan-Starling EOS, the pressure is defined as :

$$p = \rho RT\frac{1 + bp/4 + (bp/4)^2 - (bp/4)^3}{(1 - bp/4)^3} - a\rho^2 \tag{4.7}$$

with

$$a = \frac{0.4963R^2T_c^2}{p_c}$$

$$b = \frac{0.18727RT_c}{p_c}$$

The values required for the simulations are presented in Tab. (4.1) for each EOS.

4.4 Force term introduction

There are several methods to introduce the force **F** of Eq. (4.1) to which the fluid is subjected with LBM. The most common methods used to introduce the internal interaction force of the pseudo-potential model are [42]: the velocity shift, the Exact Difference Method and the Guo scheme. These three methods are briefly described below.

4.4.1 Velocity shift method

This is the original force scheme that Shan and Chen used in [21]. With this model, the force is introduced by shifting the velocity in the equilibrium distribution function. Thus,

Parameter	Peng-Robinson	Carnahan-Starling
a	2/49	1
b	2/21	4
T_c	0.072922	0.094325
ρ_c	2.657	0.13045

Table 4.1 EOS parameters for simulations

the velocity used to calculate the equilibrium distribution function is given by :

$$\mathbf{u^{eq}} = \mathbf{u} + \frac{\tau \mathbf{F}}{\rho}\delta t \tag{4.8}$$

where

$$\mathbf{u} = \sum_i f_i \mathbf{e_i} \tag{4.9}$$

In this implementation, the collision step remains unchanged. However the real fluid velocity $\mathbf{v}$ should be calculated by averaging the momentum before and after collision, and

$$\rho \mathbf{v} = \rho \mathbf{u} + \frac{\delta t}{2}\mathbf{F} \tag{4.10}$$

This method is relatively simple to implement. However, it presents stability problems as it is highly dependent on the relaxation time [43].

4.4.2 Exact Difference Method

The Exact Difference Method (EDM) was proposed in 2009 by Kupershtokh et al. [44]. Unlike the velocity shift method, EDM introduces the force by adding a discrete force term into the collision step as follows :

$$f_i(\mathbf{x} + \mathbf{e}_i\delta t, t + \delta t) - f_i(\mathbf{x}, t) = -\frac{f_i(\mathbf{x}, t) - f_i^{eq}(\mathbf{x}, t)}{\tau} + \delta t F_i(\mathbf{x}, t) \tag{4.11}$$

with

$$\delta t F_i(\mathbf{x}, t) = f_i^{eq}(\rho, \mathbf{u} + \Delta\mathbf{u}) - f_i^{eq}(\rho, \mathbf{u}) \tag{4.12}$$

Thus, the force is represented by the difference between the equilibrium distribution function calculated at two different velocities, being the variation of velocity $\Delta\mathbf{u} = \mathbf{F}\delta_t/\rho$ the change due to the body force during time step δ_t. With this method, the real fluid velocity is calculated by averaging the momentum before and after collision as in the velocity shift method :

$$\rho \mathbf{v} = \rho \mathbf{u} + \frac{\delta t}{2}\mathbf{F} \tag{4.13}$$

This method presents some advantages compared to the velocity shift such as an increased accuracy and stability as it is not a function of the relaxation time [43].

4.4.3 Guo force scheme

In Guo's force scheme [45], a discrete form of the force is introduced in the collision step and is given by :

$$F_i(\mathbf{x},t) = \left(1 - \frac{1}{2\tau}\right)\omega_i \left[\frac{\mathbf{e}_i - \mathbf{u}}{c_s^2} + \frac{\mathbf{e}_i \cdot \mathbf{u}}{c_s^4}\mathbf{e}_i\right] \cdot \mathbf{F} \tag{4.14}$$

where $\mathbf{u}$ is calculated by Eq. (4.9). With this formulation, the whole fluid velocity and equilibrium velocity used to calculate the equilibrium function distribution are the same and equal to

$$\mathbf{u^{eq}} = \mathbf{v} = \frac{1}{\rho}\left(\sum_i \mathbf{e}_i f_i + \frac{\delta t}{2}\mathbf{F}\right) \tag{4.15}$$

For its simplicity and accuracy, we will perform our simulations with the Exact Difference Method.

4.5 Test cases for validation

Two test cases are presented to validate the pseudo-potential model to simulate single-component multiphase flows: the phase separation and the verification of Laplace's law.

4.5.1 Phase separation

This test case aims to simulate the phase separation of a fluid from critical density. All the domain is initialized at zero velocity and the density is set to its critical value with a slight perturbation of 1%. The critical density can be obtained by the EOS after getting the critical temperature and pressure defined by the constants a, b, and R. For P-R and C-s EOS, critial density values can be found in Table (4.1). The temperature is fixed to a value under the critical temperature. As result, the interaction force makes the phase separation automatically when flow becomes steady. The analytical solution to this problem is given by the Maxwell construction that is obtained by the method of equal area [46]. The main idea of this method is to make equal the areas, A and B, produced by the saturated pressure on the isothermal curve of the pressure-volume phase diagram (Fig. 4.2).

$$\int_{v_l}^{v_g} p dv = p_s(v_g - v_l) \tag{4.16}$$

For this purpose, a 100×100 lattice structure was chosen to be the computational domain. The force was introduced by using the Exact Difference Method and the relaxation time was set to $\tau = 1$. The results obtained for the coexistence density curve for P-R and C-S EOS are presented in Fig. (4.3), with the simulation results from [2] with the same EOS and model

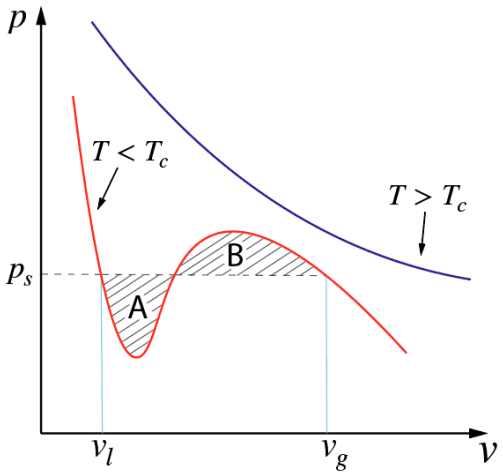

Figure 4.2 Maxwell construction

implemented.

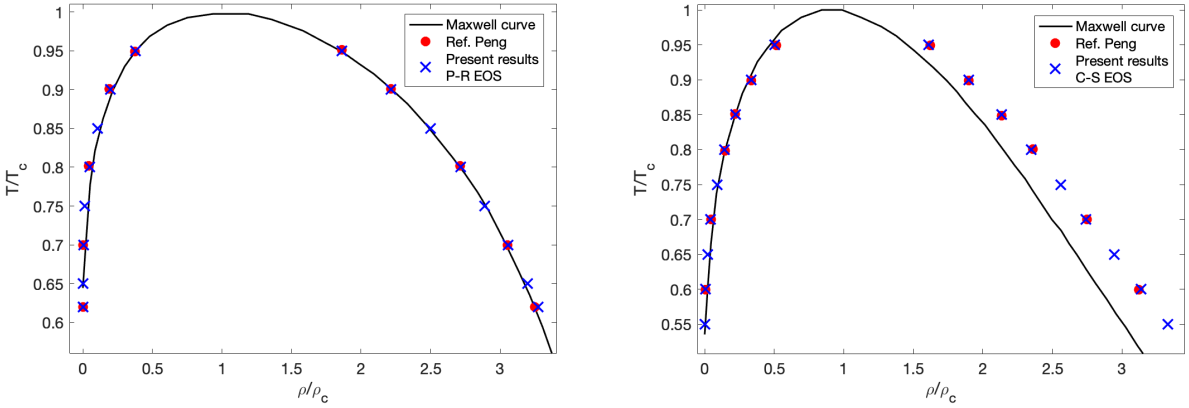

(a) (b)

Figure 4.3 Coexistence density curve for (a) P-R EOS and (b) C-S EOS, Ref. Peng [2]

The results show an excellent agreement with the simulations performed in [2], which allowed us to verify the implemented model.

Regarding the results and their comparison with the Maxwell construction [46], it is inferred that both P-R and C-S EOS perform well and agree with the analytical solution. However, it is noticed that the P-R EOS predicts the liquid phase with more accuracy than the C-S EOS. Contrarily, the C-S EOS performs better for the prediction of the vapor phase, Fig. (4.3b).

In order to compare the different methods to introduce the force into LBM, the velocity shift and EDM will be used to simulate the same test for phase separation ($T/T_c = 0.9$ with C-S EOS) and varying the relaxation time. Fig. (4.4) shows the densities of the vapor phase obtained for different relaxation times. It can be observed that the velocity shift model delivers results relatively dependent on the relaxation time by increasing the density of gas phase with the relaxation time. The stability is reduced when τ is near 0.5. It can also be noticed that for $\tau = 1$ the EDM and velocity shift are exactly equivalent. Note that this can be used to debug the code implementation for numerical accuracy. Finally, there is a slight variation of vapor density with the relaxation time for the EDM because of the curved interface. For a straight interface, the results should be exactly the same when varying τ.

4.5.2 Laplace's law

The Laplace's law determines the relationship between the pressure difference and the inverse of the radius of a water droplet or bubble. For a 2D droplet/bubble, the pressure difference between the inside and the outside pressure is given by

$$\Delta P = \frac{\sigma}{R} \tag{4.17}$$

where σ represents the surface tension. For this test, a 100×100 lattice structure has been chosen. Two EOS are used to plot the difference pressure between the inside and the outside of the water droplet while the radius increases from 14 to 24 lattice units. EDM method is used to introduce the force term into the LBM scheme and the relaxation time is set to $\tau = 1$. The pressure difference is calculated as the difference between the steady-state high pressure inside the droplet and the steady-state low pressure outside the droplet as indicated in Fig. (4.5). This pressure difference is plotted against the inverse initial radius for three different reduced temperatures of T/T_c. The values to initialize the density field are determined by the coexistence density curve that was obtained with the phase separation test at each reduced temperature. Periodic conditions are applied in all boundaries and water droplet is initialized by using a tanh function to create a diffusive layer as shown in Eq. (4.18).

$$\rho(x,y) = \frac{\rho_g + \rho_l}{2} - \frac{\rho_l - \rho_g}{2}\left[\tanh\left(\frac{2\sqrt{(x-x_0)^2 + (y-y_0)^2} - r_0}{W}\right)\right] \tag{4.18}$$

where ρ_g and ρ_l are the densities of gas and liquid phases respectively, (x_0, y_0) is the center of the droplet placed in the central position of the domain, the initial radius is r_0 and W is

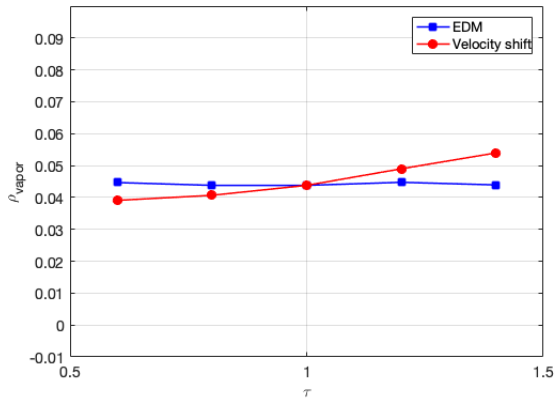

Figure 4.4 Density of vapor phase for different relaxation times

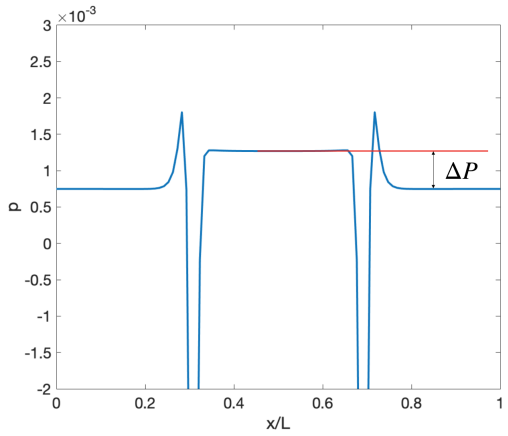

Figure 4.5 Pressure distribution along the horizontal center of the computational domain

the initial interface thickness set to 3 lattice units.

The results for both EOS P-R and C-S are presented in Fig. (4.6). They show a linear trend as expected.

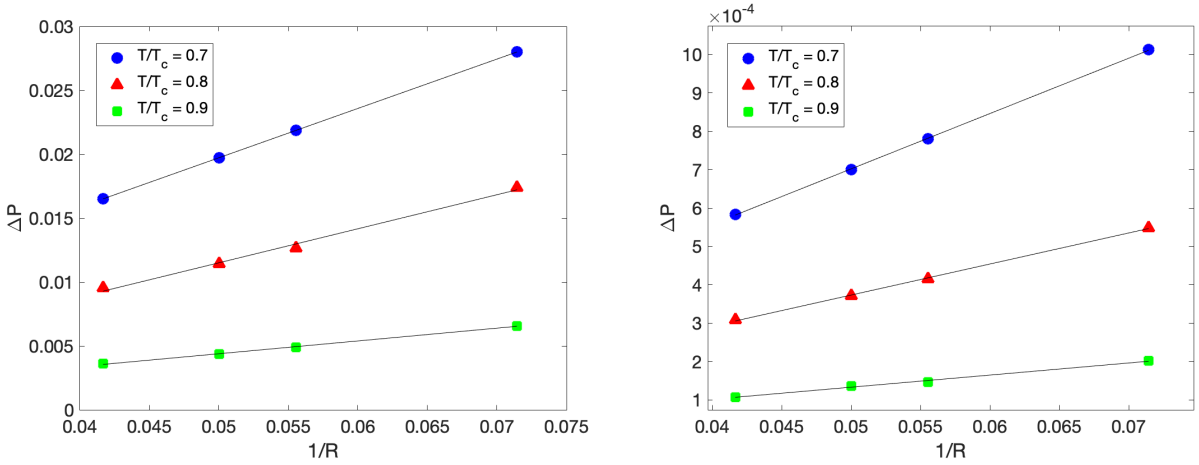

(a) (b)

Figure 4.6 Pressure difference across droplet vs. inverse radius (in lattice units) simulated at different temperatures for (a) P-R EOS and (b) C-S EOS

They show a linear relationship between the pressure difference and the inverse radius when varying the radius. It can be noticed that a decrease in the reduced temperature increases the slope of the curve which makes sense as the surface tension is increased as a consequence of a higher density ratio.

4.5.3 Spurious currents

A weakness of the pseudo-potential model is the possible presence of spurious currents, which represent the variation of velocity from the real physical situation [37]. It is important to keep these spurious currents as low as possible because their presence will influence the accuracy of the results and the stability of the method.

To evaluate the influence of these undesired velocities, a spurious Mach number will be defined as $M^s_{max} = u^s_{max}/c_s$. This value will not only help to determine how spurious currents are increased when reducing the reduced temperature, but it will also be suitable to determine when we are outside the incompressible regime for which the LBM is applicable. The test performed was the suspended droplet where the correlated physical case has a zero velocity field or zero Mach number field. In Fig. (4.7) the maximum spurious Mach number against reduced temperature is shown for P-R and C-S EOS. It can be observed that the spurious currents increase with the reduction of the reduced temperature as a consequence of the increased density ratio. The maximum spurious currents for P-R is larger than that of

the C-S for the same reduced temperature, taking into account that P-R EOS also produces higher density ratios. The dashed line represents a Mach value of 0.1. For a maximum spurious Mach number over this value, the Mach number influence is no longer negligible and the results are not valid. The velocity vectors for a specific test are presented in Fig. (4.8). It can be seen that maximum values are reached at the interface region. Ideally we should also always keep the value of spurious currents much lower than the reference velocity.

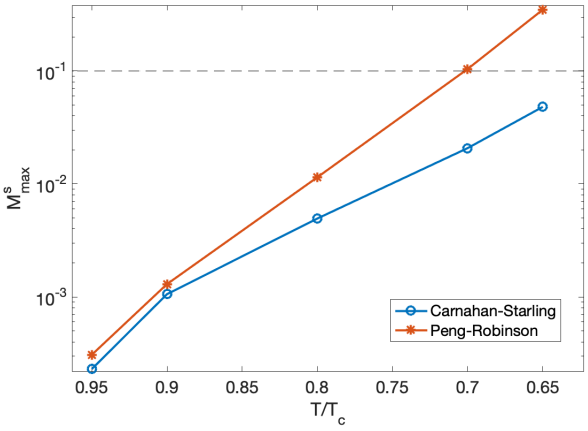

Figure 4.7 Maximum spurious currents against reduced temperature for P-R and C-S EOS

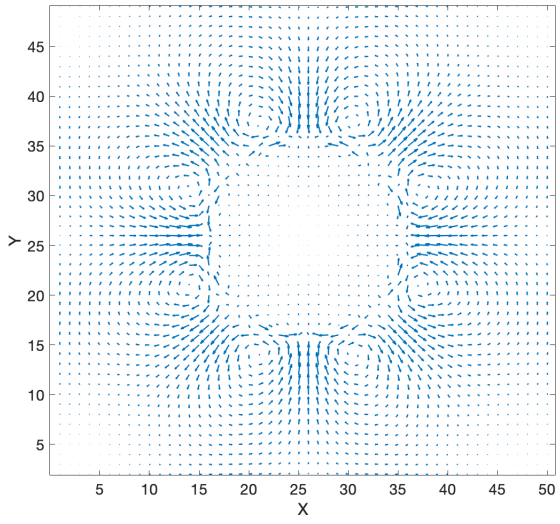

Figure 4.8 Spurious currents vectors for $T/T_c = 0.75$ and C-S EOS

CHAPTER 5 THERMAL LATTICE BOLTZMANN METHOD FOR ADVECTION-DIFFUSION EQUATIONS

5.1 Fundamentals of thermal LBM

The LBM can also be used to solve a simplified energy equation and calculate the evolution of the temperature of a fluid. If the viscous heat dissipation and the compression work carried out by the pressure are negligible, the temperature field is passively advected by the fluid flow and obeys a simpler passive-scalar equation [32] :

$$\frac{\partial T}{\partial t} + \nabla \cdot (\mathbf{u}T) = \alpha \nabla^2 T \tag{5.1}$$

This convection-diffusion equation can be solved by LBM by modeling the temperature field with fictive particles, which stream and collide over a discrete lattice, the aforementioned particle distribution functions. A BGK model will be implemented in a D2Q5 lattice structure as shown in Fig. (5.1). The lattice BGK equation for the Eq. (5.1) is given by

$$g_i(\mathbf{x} + \mathbf{e}_i\delta_t, t + \delta_t) - g_i(\mathbf{x}, t) = -\frac{\delta_t}{\tau_T}(g_i(\mathbf{x}, t) - g_i^{eq}(\mathbf{x}, t)) \tag{5.2}$$

where τ_T is the single thermal relaxation time, g_i is the temperature distribution function and g_i^{eq} is the equilibrium value given by

$$g_i^{eq}(T, \mathbf{u}) = T\omega_i \left[1 + \frac{\mathbf{e}_i \cdot \mathbf{u}}{c_s^2}\right] \tag{5.3}$$

The fluid temperature is calculated from the temperature distribution function :

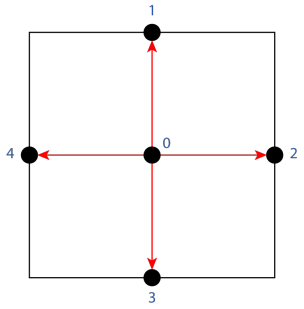

Figure 5.1 D2Q5 lattice stencil. The square denoted by black lines has an edge length $2\delta x$. Velocities are represented in red and rest velocity vector $\bar{\mathbf{e}}_0 = 0$ is not shown

$$T = \sum_i g_i \tag{5.4}$$

From this BGK lattice Boltzmann equation, Eq. (5.1) can be derived through the Chapman-Enskog procedure [32]. This procedure provides the relation between the thermal diffusivity and the single relaxation time :

$$\alpha = \frac{(2\tau_T - 1)}{4}\frac{\delta x^2}{\delta t} \tag{5.5}$$

As mentioned for the velocity field, the lattice speed is given by $c = \frac{\delta x}{\delta t}$ and for simplicity we consider a system of units with $\delta x = \delta t = 1$, i.e. the so-called lattice units.

5.2 Hot plate diffusion

To test the ability of the LBM to solve the convection-diffusion equation, we consider the temperature distribution development near a semi-infinite plate as shown in Fig. (5.2). A uniform fluid velocity u_0 is assumed along the x-axis and a constant temperature at the surface of the plate T_p. The remaining open boundaries are modelled by Dirichlet, zero

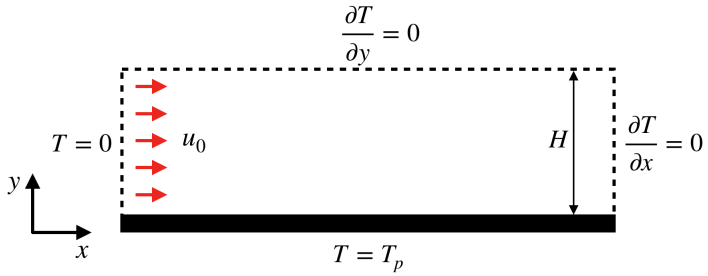

Figure 5.2 Sketch of simulation domain for the semi-infinite plate problem

temperature at the inlet, and Neumann conditions for the top and the outlet. The heat flux is assumed to be zero at these boundaries [32]. For the stationary situation and taking into account the choice of axis directions, the governing equation is :

$$\frac{\partial T}{\partial x}u_0 = \alpha\frac{\partial^2 T}{\partial y^2} \tag{5.6}$$

where it has been considered that the diffusion along the x-axis is negligible compared to its advection as the Péclet number, Pe (defined in Eq. (5.7)), is high.

$$\mathrm{Pe} = \frac{Hu_0}{\alpha} \tag{5.7}$$

The analytical solution of this equation is given by :

$$T(x,y) = T_p \cdot \text{erfc}\left(\frac{y}{\sqrt{4\alpha x/u_0}}\right) \tag{5.8}$$

where $\text{erfc}(x)$ is the complementary error function :

$$\text{erfc}(x) = 1 - \text{erf}(x) = \frac{2}{\pi}\int_x^\infty e^{-x'^2}dx' \tag{5.9}$$

We perform a simulation on a D2Q5 lattice with $L \times H = 200 \times 40$ nodes, with a uniform fluid velocity of $u_0 = 0.1$ and a Péclet number of $\text{Pe} = 106$. The temperature at the plate is set to be $T_p = 1$ and the thermal diffusivity α is determined by the Péclet number. Fig. (5.3) shows the temperature profile and comparisons with the analytical solution for the steady state. The simulation results agree well with the analytical solution which allows to verify the ability of LBM to solve stationary convection-diffusion problems under certain conditions.

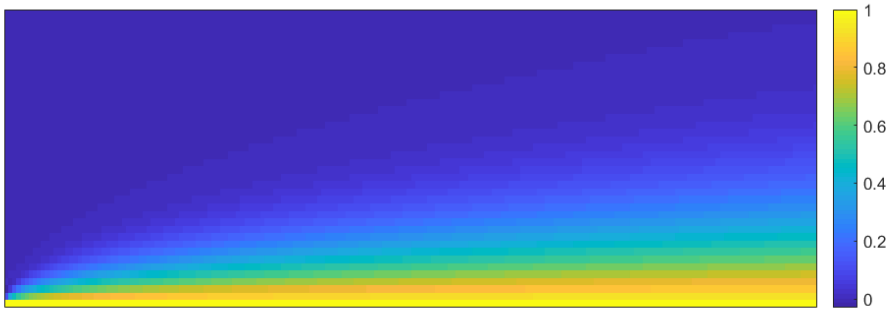

(a)

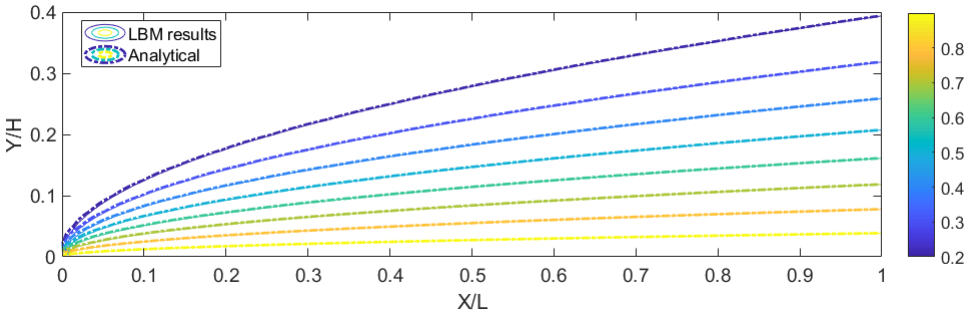

(b)

Figure 5.3 (a) Temperature distribution at steady state for the semi-infinite plate. (b) Comparisons of the temperature distribution at steady state between the LBM results and analytical solution

CHAPTER 6 PHASE CHANGE MODEL

6.1 Introduction

While simulating the process of a water droplet impact and freezing, the droplet temperature is in a metastable state below the freezing point before its impact on the surface. Once the contact is made, its temperature raises to the freezing temperature because of the released latent heat. At this temperature, phase change occurs governed by the heat transfer. When the droplet is completely frozen, its temperature decreases down to a value near the wall temperature, which is considered to be constant all the time. To simulate this process, besides the multi-phase model, a phase change model is also required.

As it has already been mentioned in the literature review, the LBM seems a promising model for simulating phase change as the liquid-solid interface can be determined automatically in a simple way. Among the alternative models for simulating phase change with LBM, enthalpy based methods have been chosen to simulate phase change in this study for their simple application and good accuracy.

6.2 Total enthalpy method

The continuity, momentum and energy conservation equations for a phase change material considering a laminar, incompressible and Newtonian flow, are presented as :

$$\frac{\partial \rho}{\partial t} + \nabla \cdot (\rho \mathbf{u}) = 0 \tag{6.1}$$

$$\frac{\partial (\rho \mathbf{u})}{\partial t} + \nabla \cdot (\rho \mathbf{u}\mathbf{u}) = -\nabla p + \nabla \cdot (\mu \nabla \mathbf{u}) + \mathbf{F} \tag{6.2}$$

$$\frac{\partial (\rho C_p T)}{\partial t} + \nabla \cdot (\rho C_p T \mathbf{u}) = \nabla \cdot (\lambda \nabla T) - \frac{\partial (\rho h_{sl} f_l)}{\partial t} - \nabla \cdot (\rho h_{sl} f_l \mathbf{u}) \tag{6.3}$$

where ρ, $\mathbf{u}$, p, μ denote the density, velocity, pressure and dynamic viscosity of the fluid, the temperature is T and C_p, λ, f_l, h_{sl} are the specific heat, thermal conductivity, liquid fraction and latent heat of phase change material as shown in Fig. (6.1). The subscript l refers to the liquid phase, whereas s refers to the solid phase. In energy Eq. (6.3), a source term q

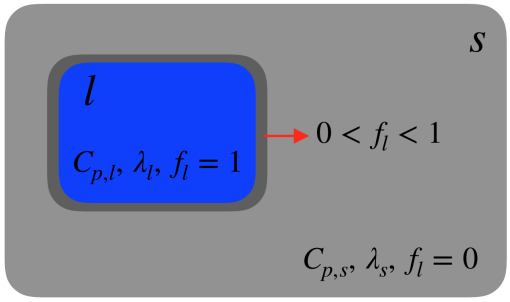

Figure 6.1 Schematic of a phase change material

caused by the absorption or release of latent heat has been introduced :

$$q = -\left[\frac{\partial(\rho h_{sl} f_l)}{\partial t} + \nabla \cdot (\rho h_{sl} f_l \mathbf{u})\right] \tag{6.4}$$

The enthalpy method for phase change uses the enthalpy to solve the temperature field and track the interface. The total enthalpy is defined as :

$$H = C_p T + f_l h_{sl} \tag{6.5}$$

where $C_p T$ represents the sensible enthalpy and $f_l h_{sl}$ the latent enthalpy. The volume-phase liquid fraction f_l is used to capture the interface as it is zero for the solid region and unity for the liquid region. The phase interface is defined when $0 < f_l < 1$.

The last term in the energy conservation equation $\nabla \cdot (\rho h_{sl} f_l \mathbf{u})$ is neglected as the phase change zone (known as mushy zone) is considered to act like solid [24]. The energy conservation equation becomes as shown below :

$$\frac{\partial(\rho C_p T)}{\partial t} + \nabla \cdot (\rho C_p T \mathbf{u}) = \nabla \cdot (\lambda \nabla T) - \frac{\partial(\rho h_{sl} f_l)}{\partial t} \tag{6.6}$$

The LBM is used to solve this equation and perform a phase change simulation of the fluid which is achieved with the total enthalpy method proposed by Huang and Wu in 2013 [47].

The total enthalpy energy equation is obtained from the presented energy equation by combining the latent heat source $\partial(\rho h_{sl} f_l)/\partial t$ into the transient term $\partial(\rho C_p T)/\partial t$ taking into account the definition of the total enthalpy previously presented in Eq. (6.6). Note that

density is considered to be constant in Eq. (6.7).

$$\frac{\partial H}{\partial t} + \nabla \cdot (C_p T \mathbf{u}) = \nabla \cdot \left(\frac{\lambda}{\rho} \nabla T \right) \tag{6.7}$$

In order to apply the LBM to solve this energy equation, a SRT lattice Boltzmann equation is considered for the total enthalpy H.

$$g_i(\mathbf{x} + \mathbf{e}_i \delta_t, t + \delta_t) = g_i(\mathbf{x}, t) - \frac{1}{\tau_T} \left[g_i(\mathbf{x}, t) - g_i^{eq}(\mathbf{x}, t) \right] \tag{6.8}$$

where g is the distribution function for the total enthalpy and τ_T is the single relaxation time. Considering a two-dimensional representation with a typical D2Q9 lattice stencil, the equilibrium distribution function can be introduced as [24]:

$$g_i^{eq} = \begin{cases} H - C_{p,\mathrm{ref}} T + \omega_i C_p T \left(\frac{C_{p,\mathrm{ref}}}{C_p} - \frac{\mathbf{I}:\mathbf{uu}}{2c_s^2} \right), & i = 0 \\ \omega_i C_p T \left[\frac{C_{p,\mathrm{ref}}}{C_p} + \frac{\mathbf{e}_i \cdot \mathbf{u}}{c_s^2} + \frac{(\mathbf{e}_i \mathbf{e}_i - c_s^2 \mathbf{I}):\mathbf{uu}}{2c_s^4} \right], & i \neq 0 \end{cases} \tag{6.9}$$

where $C_{p,\mathrm{ref}}$ is the reference specific heat which is constant over the entire space and allows to introduce different specific heat and thermal conductivity for the liquid and solid phase.

The total enthalpy is then calculated as :

$$H = \sum_{i=0}^{8} g_i \tag{6.10}$$

The followings relations are used to calculate liquid fraction and temperature

$$f_l = \begin{cases} 0, & H \leq H_s \\ \dfrac{H - H_s}{H_l - H_s}, & H_s \leq H \leq H_l \\ 1, & H \geq H_l \end{cases} \tag{6.11}$$

$$T = \begin{cases} T_s - \dfrac{H_s - H}{C_{p,s}}, & H \leq H_s \\ \dfrac{H_l - H}{H_l - H_s} T_s + \dfrac{H - H_s}{H_l - H_s} T_l, & H_s \leq H \leq H_l \\ T_l + \dfrac{H - H_l}{C_{p,l}}, & H \geq H_l \end{cases} \tag{6.12}$$

with $H_s = C_{p,s} T_s$ the total enthalpy at solid temperature and $H_l = C_{p,l} T_l + h_{sl}$ the total enthalpy at the liquidus temperature T_l. The specific heat of the solid and liquid phases are

$C_{p,s}$ and $C_{p,l}$, respectively. The phase change is considered to happen at a constant temperature, so $T_s = T_l = T_m$, with T_m the melting or freezing temperature.

The relationship between the thermophysical properties and the single relaxation time is obtained from the Chapman-Enskog analysis and it can be written as follows

$$\frac{\lambda}{\rho C_{p,\text{ref}}} = c_s^2(\tau_T - 0.5)\delta_t \tag{6.13}$$

As noted by authors [24], the choice of $C_{p,\text{ref}}$ is arbitrary and the harmonic mean of $C_{p,l}$ and $C_{p,s}$ was used as it was numerically stable based on their simulations.

$$C_{p,\text{ref}} = \frac{2C_{p,s}C_{p,l}}{C_{p,s} + C_{p,l}} \tag{6.14}$$

It should be pointed out that the presented method does not need to iterate at every time step to solve the thermal LBE as the latent heat source term has been combined with the transient term. This approach eliminates the source term in the lattice Boltzmann equation so that it is no longer implicit as it happens in the method of Jiaung et al. [26].

Regarding the boundary conditions, only Dirichlet and Neumann conditions will be applied in the thermal model to fix a constant temperature or flux, respectively.

6.3 Test cases for verification

The verification of the phase change model is made through different well-known benchmark tests for which either an analytical solution or numerical references are available. We will only consider in this section the thermal model so the involved velocity field is steady at every time step and consequently the energy conservation Eq. (6.3) is uncoupled from the continuity and momentum equations, Eqs. (6.1) and (6.2), respectively. This means that only conduction is involved during the phase change and convection is not considered. In the next section, the coupled density and thermal model will be presented.

To demonstrate the accuracy and feasibility of the presented method to simulate solid-liquid phase change, the Stefan problem will be solved for three different tests. First, we will consider two one-dimensional phase change problems. Then, a two-dimensional test will be performed in a square domain.

6.3.1 One-region phase change Stefan problem

The first test is the one dimensional one-region melting by conduction. 'One-region' refers to the fact that all the domain starts at the melting temperature $T_m = 0$ uniformly solid. Then at the initial time step, the left wall temperature is raised to a constant value $T_w = 1$ higher than T_m. This change drives the start of the melting process in which only the liquid phase is active while the solid one remains at a constant temperature T_m. The heat transfer over the interface makes the evolution of the melting process.
Regarding the boundary conditions, a Dirichlet boundary condition is applied to keep the wall temperature constant. The domain is considered to be infinite in x axis: in order to do that with a finite length L, we consider a large number of lattices in that direction and we must assure that at the evaluation time step, the temperature at the right wall is fixed at T_m and with a zero slope as adiabatic boundary condition is applied. A schematic of this test case is depicted in Fig. (6.2).

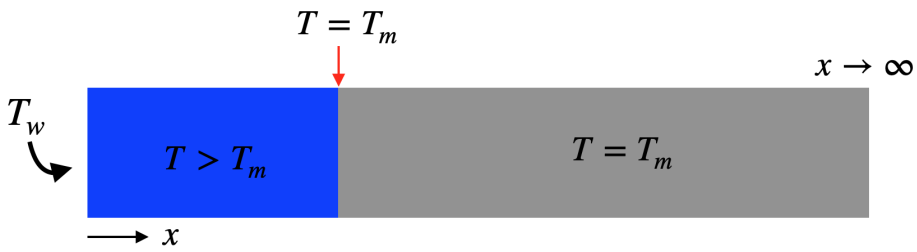

Figure 6.2 Schematic of the one-dimensional one-region melting by conduction

This test case is characterized by the dimensionless parameter known as Stefan number which relates the sensible heat to the latent heat and is defined as $\mathrm{Ste}_l = C_{p,l}(T_w - T_m)/h_{sl}$. The analytical solution for the evolution of the temperature field over time is given by the following expression :

$$T(\mathbf{x},t) = \begin{cases} T_w - \dfrac{T_w - T_m}{\mathrm{erf}(k)}\mathrm{erf}\left(\dfrac{x}{2\sqrt{\lambda_l/(\rho C_{p,l})t}}\right), & 0 \le x \le s(t) \\ T_m, & x > s(t) \end{cases} \tag{6.15}$$

where $\mathrm{erf}(x)$ is the error function Eq. (6.17) and $s(t)$ defines the interface location which is given by the following expession :

$$s(t) = 2k\sqrt{\frac{\lambda_l}{\rho C_{p,l}}t} \tag{6.16}$$

$$\mathrm{erf}(x) = \frac{1}{\sqrt{\pi}} \int_{-x}^{x} e^{-t^2} dt \tag{6.17}$$

where k is a parameter which can be obtained by solving the following transcendal equation :

$$\frac{\mathrm{Ste}_l}{\exp(k^2)\mathrm{erf}(k)} = k\sqrt{\pi} \tag{6.18}$$

The simulation parameters used for the performed tests are : $N_x = 128$, $T_w = 1$, $T_m = 0$, $\rho = 1$, $C_{p,l} = C_{p,s} = 1$, $\lambda_l = 1/6$. Note that, as the solid phase is not active, the value $\lambda_s = 1/6$ does not influence in the simulation. The relaxation time is chosen to be $\tau_T = 1$ and the Stefan number is $\mathrm{Ste}_l = 0.01$. The temperature distribution and location of solid-liquid interface with the analytical solution are shown in Fig. (6.3). The results are presented with the following dimensionless variables :

$$T^* = \frac{T - T_w}{T_m - T_w}; \quad t^* = \frac{\alpha_l t}{L^2}; \quad x^* = \frac{x}{L}; \quad s^* = \frac{s}{L} \tag{6.19}$$

Fig. (6.3a) represents the temperature distribution for several time steps. It can be inferred

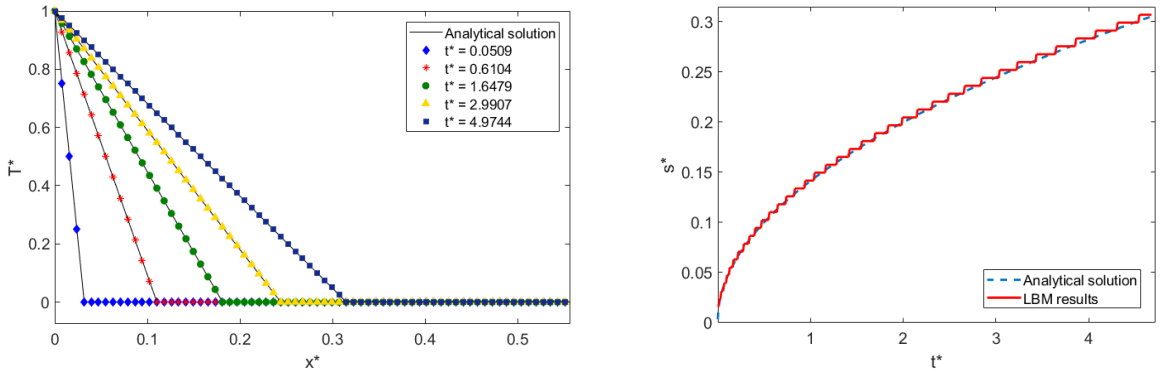

(a) (b)

Figure 6.3 Comparisons between analytical solution and LB model for (a) the temperature distribution and (b) the interface position for one-phase change problem in dimensionless variables Eq. (6.19)

that the LB results agree with the analytical solution. The evolution of the temperature is almost linear from the wall temperature to the melting temperature where the solid phase is present. As it has been explained before, the solid phase remains inactive and at a constant temperature. The evolution of the liquid-solid interface is presented in Fig. (6.3b) where it can be noticed that the LB simulation results follow with accuracy the interface evolution over time. The staggered shape of the LB results is explained by taking into account that the interface is a lattice wide, so the interface remains in the same position for several time

steps until it continues to the next one.

6.3.2 Two-region phase change Stefan problem

For the two-region melting problem, the substance starts solid at a temperature T_i which is lower than the melting temperature ($T_i < T_m$). Then the left wall temperature is abruptly raised to a constant temperature higher than T_m. As the solid phase is at a different temperature from the melting temperature, two phases are active. The heat flux passes through the interface from the liquid phase and is transferred sequentially in the solid phase.

The same boundary conditions used for the previous test have been applied and the consideration of the infinite domain needs to be kept in mind as well. As the solid phase is also active, we need to assure that the solutions extracted always verify that $T(\infty, t) = T_i$.

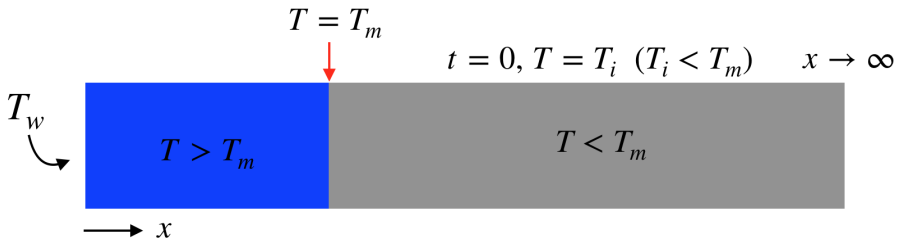

Figure 6.4 Schematic of the one-dimensional two-region melting by conduction

For this test, two dimensionless Stefan numbers, one for each phase, are defined : $\mathrm{Ste}_l = C_{p,l}(T_w - T_m)/h_{sl}$ and $\mathrm{Ste}_s = C_{p,s}(T_m - T_i)/h_{sl}$. The analytical solution is :

$$T(\mathbf{x}, t) = \begin{cases} T_w - \dfrac{T_w - T_m}{\mathrm{erf}(k)} \mathrm{erf}\left(\dfrac{x}{2\sqrt{\lambda_l/(\rho C_{p,l})t}}\right), & 0 \leq x \leq s(t) \\ T_i + \dfrac{T_m - T_i}{\mathrm{erfc}(k/\sqrt{R_\alpha})} \mathrm{erfc}\left(\dfrac{x}{2\sqrt{\lambda_s/(\rho C_{p,s})t}}\right), & x > s(t) \end{cases} \tag{6.20}$$

where $\mathrm{erfc}(x) = 1 - \mathrm{erf}(x)$ is the complementary error function and $R_\alpha = \alpha_s/\alpha_l$ is the ratio of the thermal diffusivities of the two phases. The interface position is given by :

$$s(t) = 2k\sqrt{\frac{\lambda_l}{\rho C_{p,l}} t} \tag{6.21}$$

which is the same expression used for one-region Stefan problem, but for this case, the

parameter k is the solution of the following equation :

$$\frac{\mathrm{Ste}_l}{\exp(k^2)\mathrm{erf}(k)} - \frac{\mathrm{Ste}_s\sqrt{R_\alpha}}{\exp(k^2/R_\alpha)\mathrm{erfc}(k/\sqrt{R_\alpha})} = k\sqrt{\pi} \tag{6.22}$$

For this test, we will first consider the same thermodynamic properties for both phases, i.e., $C_{p,l} = C_{p,s}$ and $\lambda_l = \lambda_s$. So, the simulation parameters used are : $N_x = 768$, $T_i = 0$, $T_w = 1$, $T_m = 0.5$, $\rho = 1$, $C_{p,l} = 1$, $\lambda_l = 1/6$, $R_{C_p} = C_{p,s}/C_{p,l} = 1$, $R_\lambda = \lambda_s/\lambda_l = 1$. The Stefan number is set to 0.005 and the relaxation time to unity. The temperature distribution and the location of the interface are shown in Fig. (6.5) for these simulation parameters.

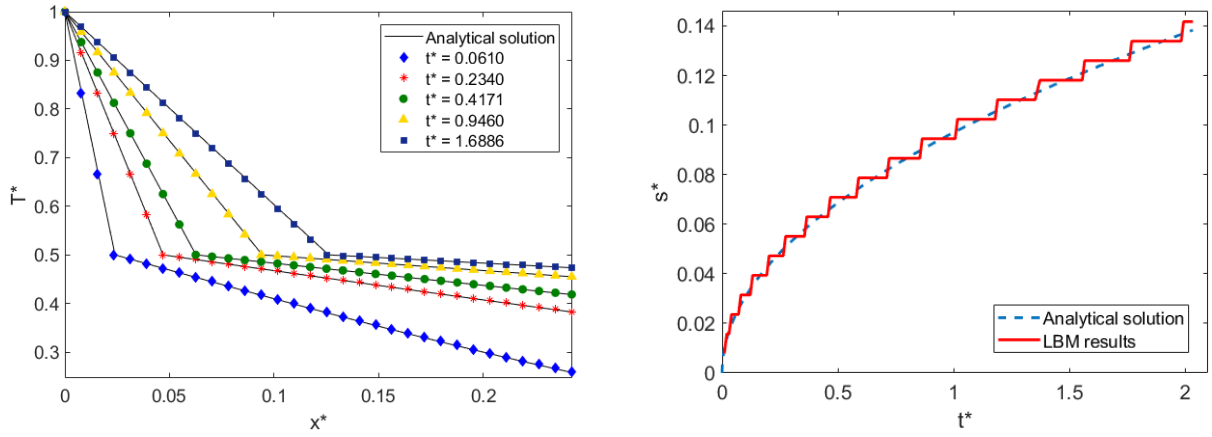

(a) (b)

Figure 6.5 Comparisons between analytical solution and LB model for (a) the temperature distribution and (b) the interface position for two-phase change problem, $R_{C_p} = 1$, $R_\lambda = 1$ in dimensionless variables Eq. (6.19)

Figure 6.5 shows a good agreement between the simulation results and the analytical solution for the two-region problem with the same thermodynamic properties. The temperature changes follow a linear behavior from the wall to the melting temperature where the interface is located. Then, it continues to decrease changing the slope until zero where it finally reaches the initial temperature of the solid. Regarding the interface evolution, the LB results follow the evolution of the interface over time with good precision.

Most enthalpy-based LB models for solid-liquid phase change are not accurate when simulating solid and liquid phases with different thermodynamic properties because the thermal conductivity and specific heat are coupled through the thermal diffusivity. As this one is simulated by a LB model, when C_p changes from one phase to another, the temperature and heat flux conditions can not be satisfied at the same time [24]. The introduction of a refer-

ence specific heat $C_{p,\text{ref}}$ in the equilibrium distribution function for enthalpy provides the total enthalpy model the ability to simulate phase change with differences in both thermal conductivity and specific heat between two phases. We consider then the same parameters used in the previous test but now we change the thermodynamics properties by setting $R_{C_p} = 4$ and $R_\lambda = 2$. When we change these properties, the relaxation times for liquid and solid phases are different, the relaxation time for the solid phase is determined by $\tau_{Ts} = R_\lambda(\tau_{Tl} - 0.5) + 0.5$. The simulation results are presented in Fig. (6.6).

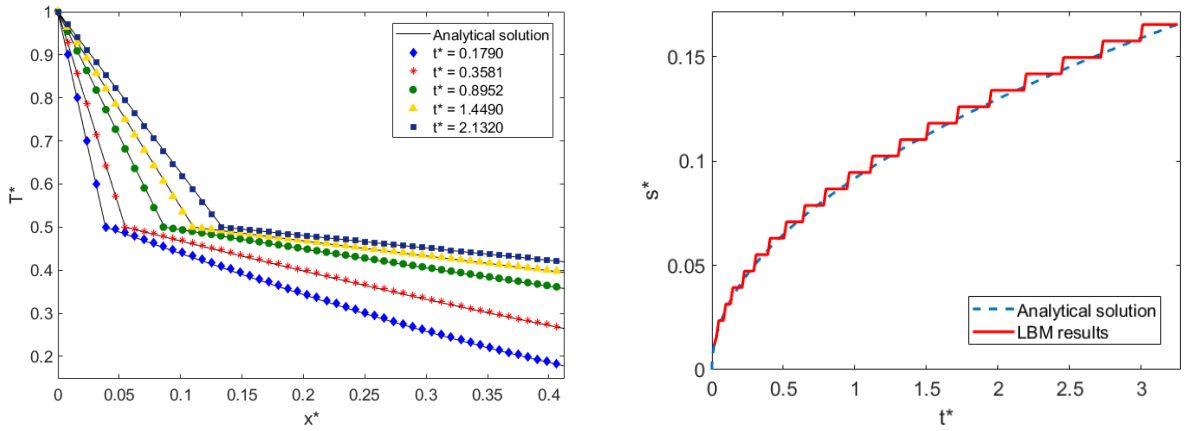

(a) (b)

Figure 6.6 Comparisons between analytical solution and LB model for (a) the temperature distribution and (b) the interface position for two-phase change problem, $R_{C_p} = 4$, $R_\lambda = 2$ in dimensionless variables Eq. (6.19)

Both the temperature distribution and interface evolution over time show a good agreement with the analytical solution. The evolution of temperature is similar to the previous test. For this simple scenario, the ability of the presented model to simulate phase change with different thermophysical properties for both phases is demonstrated.

6.3.3 Solidification of a semi-infinite square

In order to further validate the proposed model, a solidification dominated by conduction from a corner in a quarter-space is simulated as shown in Fig. (6.7). The liquid starts at a uniform temperature T_i higher than the freezing temperature T_f. At $t = 0$, the temperature of the south and left walls are lowered to a constant value T_w below the freezing temperature. Adiabatic boundary conditions are applied in the top and right boundaries. For this test, we need to take into account the same consideration for the infinite boundary conditions simulated by an adiabatic boundary. The initial temperature is $T_i = 0.3$, while constant

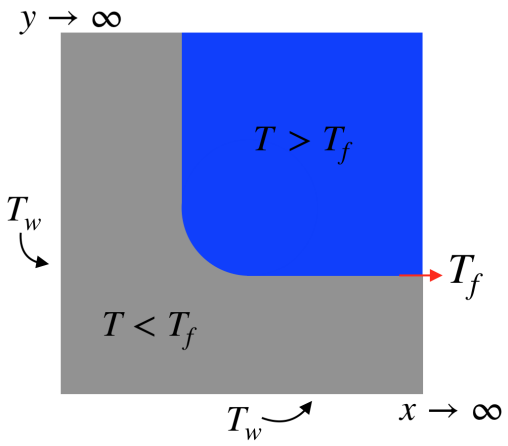

Figure 6.7 Schematic of solidification from a corner in a quarter-space

temperature boundaries are set to $T_w = -1$. The freezing temperature value is between T_i and T_w and is fixed to $T_f = 0$. The remaining parameters are as follows : $C_{p,l} = C_{p,s} = 1$, $\lambda_l = \lambda_s = 1$, Stefan number $\mathrm{Ste}_l = \mathrm{Ste}_s = C_{p,l}(T_m - T_w)/h_{sl} = 4$. Comparisons with the analytical solution provided in [48] for the phase interface position and the isothermal lines is presented in Fig. (6.8) at $t^* = 0.25$. The results show a good agreement with the reference, thus verifying the ability of the presented method to simulate phase change in two dimensional cases.

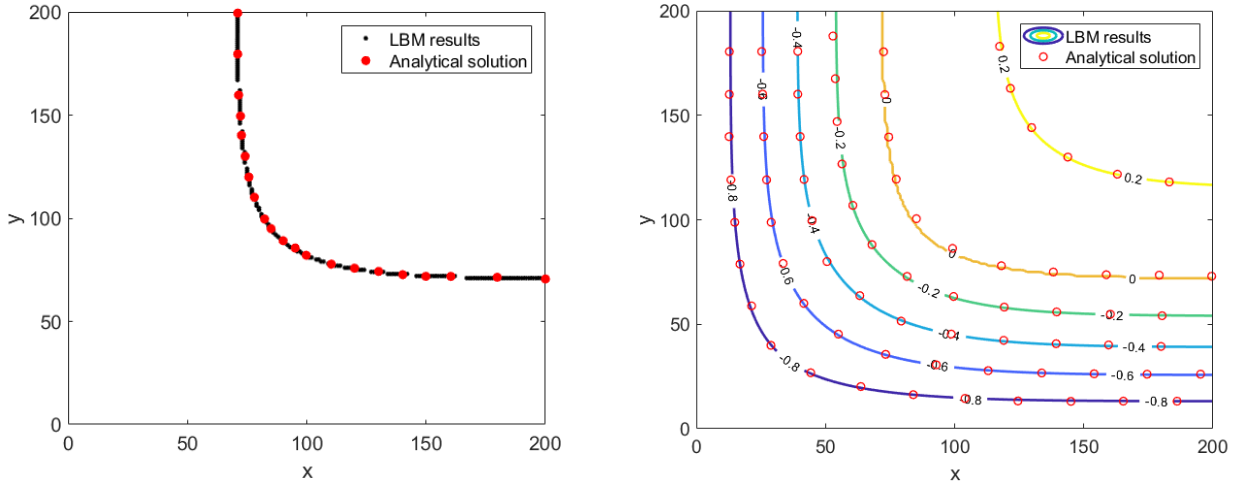

(a) (b)

Figure 6.8 Comparisons between analytical solution and LB model for the position of (a) the interface and (b) the isotherms $T^* = 0.2, 0, -0.2, -0.4, -0.6, \text{and} -0.8$ at $t^* = 0.25$

6.4 Coupled thermal and fluid model

The previous description of the thermal model with phase change has been made without considering the solution of the continuity and momentum equations. In order to get the solution of the complete system, a double-distribution-function approach is used : one for the density and one for the enthalpy.

The coupling is made through the equilibrium distribution function and the Boussinesq approximation which assumes that all the fluid properties can be considered as constant except in the body force term, where the fluid density is assumed to be a linear function of the temperature [45] :

$$\mathbf{F} = -\rho \mathbf{g}(T - T_{ref}) \tag{6.23}$$

Apart from the force term addition, a non-slip velocity boundary condition is applied at the moving interface. This can be solved by applying the Immersed moving Boundary Scheme (IBS) which has been used for the simulation of particles suspension proposed by Noble and Torczynski [49]. This scheme is implemented by modifying the lattice Boltzmann equation for the density distribution function as follows :

$$f_i(\mathbf{x} + \mathbf{e}_i\delta_t, t + \delta_t) = f_i(\mathbf{x}, t) - \frac{1 - B}{\tau}\left[f_i(\mathbf{x}, t) - f_i^{eq}(\mathbf{x}, t)\right] + B\Omega_i^s + (1 - B)\delta t F_i \tag{6.24}$$

where B is a weighting function defined as :

$$B = \frac{(1 - f_l)(\tau - 0.5)}{f_l + \tau - 0.5} \tag{6.25}$$

and Ω_i^s is defined as an additional collision term which bounces back the non-equilibrium part of the distribution function :

$$\Omega_i^s = f_{\bar{i}}(\mathbf{x}, t) - f_i(\mathbf{x}, t) + f_{\bar{i}}^{eq}(\rho, \mathbf{u}_s) - f_i^{eq}(\rho, \mathbf{u}) \tag{6.26}$$

where $\bar{i}$ indicates the opposite direction of i and $\mathbf{u}_s$ represents the solid velocity ($\mathbf{u}_s = 0$ for our tests).

If the lattice is liquid ($f_l = 1$, $B = 0$), the original LBE is recovered and we have :

$$f_i(\mathbf{x} + \mathbf{e}_i\delta_t, t + \delta_t) = f_i(\mathbf{x}, t) - \frac{1}{\tau}\left[f_i(\mathbf{x}, t) - f_i^{eq}(\mathbf{x}, t)\right] + \delta t F_i \tag{6.27}$$

On the contrary, if the lattice is solid ($f_l = 0$, $B = 1$), the LBE turns into the following expression which represents the bounce-back of the non-equilibrium part of the distribution function :

$$f_i(\mathbf{x} + \mathbf{e}_i\delta_t, t + \delta_t) = f_{\bar{i}}(\mathbf{x}, t) + f_{\bar{i}}^{eq}(\rho, \mathbf{u}_s) - f_i^{eq}(\rho, \mathbf{u}) \tag{6.28}$$

6.4.1 Phase change with natural convection

All the previous problems consider a steady situation for the fluid so that the energy conservation equation is uncoupled. To further verify the proposed method for the phase change, the melting process by natural convection in a square cavity is simulated.

The substance starts uniformly solid at the melting temperature T_m. Then at $t = 0$, the left wall temperature is raised to a constant temperature T_h higher than the melting temperature and, at the same time the right wall is kept to a constant value T_c which is equal to the melting temperature. The north and south walls are adiabatic as shown in Fig. (6.9). The following assumptions are applied : the fluid is considered to be incompressible, the Boussinesq approximation is applicable for the liquid and the thermophysical properties for both phases are equal and constant. The following dimensionless parameters are used :

$$\mathrm{Ste} = \frac{C_{p,l}(T_h - T_m)}{h_{sl}};\ \ \mathrm{Ra} = \frac{g\beta(T_h - T_m)L^3}{\nu\alpha};\ \ \mathrm{Pr} = \frac{\nu}{\alpha}\ \ \mathrm{Fo} = \frac{\alpha_l t}{L^2} \tag{6.29}$$

where Ste is the Stefan number, Ra is the Rayleigh number, Pr the Prandtl number and Fo is the Fourier number to define a dimensionless time. The average Nusselt number at the left wall is defined by the following expression in lattice units :

$$\mathrm{Nu}_{ave} = \int_0^L \left.\frac{\partial T}{\partial x}\right|_{x=0} dy \approx \sum_{j=1}^{N_y}(T_{0,j} - T_{1,j}) \tag{6.30}$$

The simulation parameters chosen for this test are the following : $N_x = N_y = 150$, $T_h = 1$, $T_m = T_c = 0$, $C_{p,l} = C_{p,s} = 1$, $\lambda_l = \lambda_s = 1/6$, $\rho_0 = 1$, $\mathrm{Ste} = 0.01$, $\mathrm{Pr} = 0.02$, $\tau_l = 1$. Two different Rayleigh numbers are considered : $\mathrm{Ra} = 25000$ and $\mathrm{Ra} = 250000$. The simulation results of this LB model are compared with those of Mencinger [3] where the same problem is solved by using an adaptive grid.

The temperature field at different Fourier numbers is presented in Fig. (6.10) for both Ra values. We can observe that conduction is the prevailing heat transfer mechanism at the beginning as the interface remains almost parallel to the left wall. But when the liquid phase

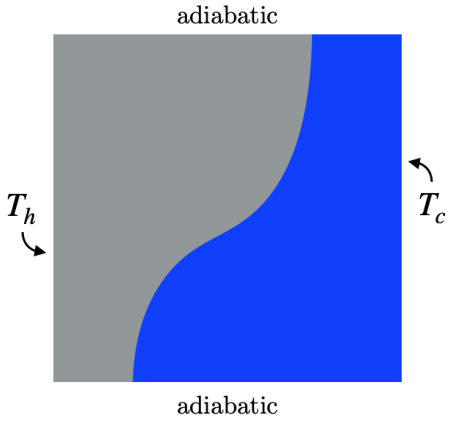

Figure 6.9 Schematic of phase change by convection.

becomes thicker, the convection is increased and the top of the cavity melts faster as more heat is transferred to the upper region because of a clockwise circulation of the fluid. By comparing the results for two Ra numbers, it can be inferred that a higher Ra number leads to more vortices and an increased rate of melting.

The positions of the liquid-solid interface at different Fo numbers are presented in Fig. (6.11). The comparison with the results provided in [3] show a good agreement with the reference.

The variations of the total liquid fraction and the average Nusselt number along the left wall are shown in Figs. (6.12) and (6.13). The results agree well with the reference.

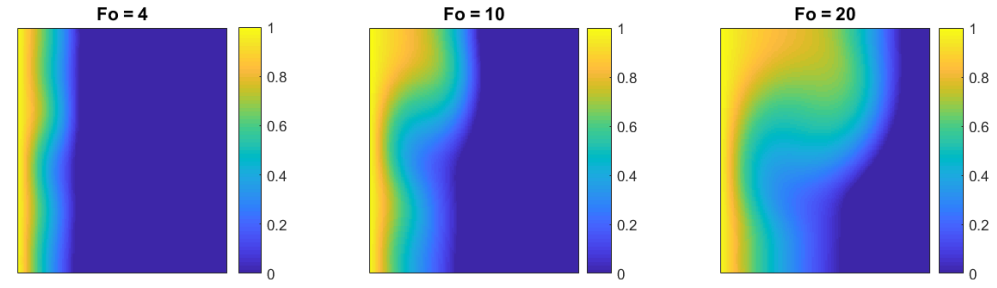

(a)

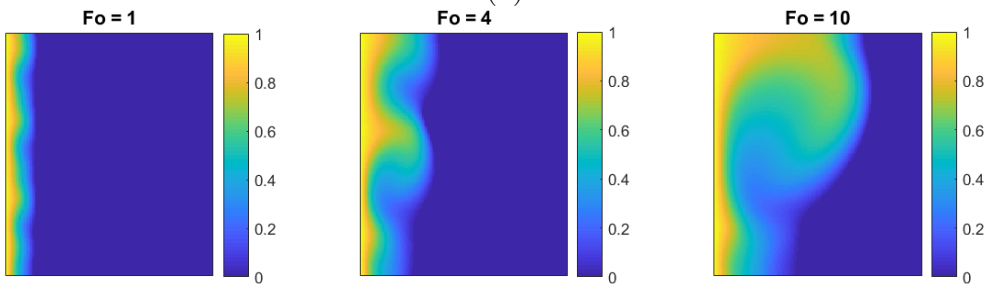

(b)

Figure 6.10 Temperature field at different Fourier numbers for (a) Ra = 25000 and (b) Ra = 250000

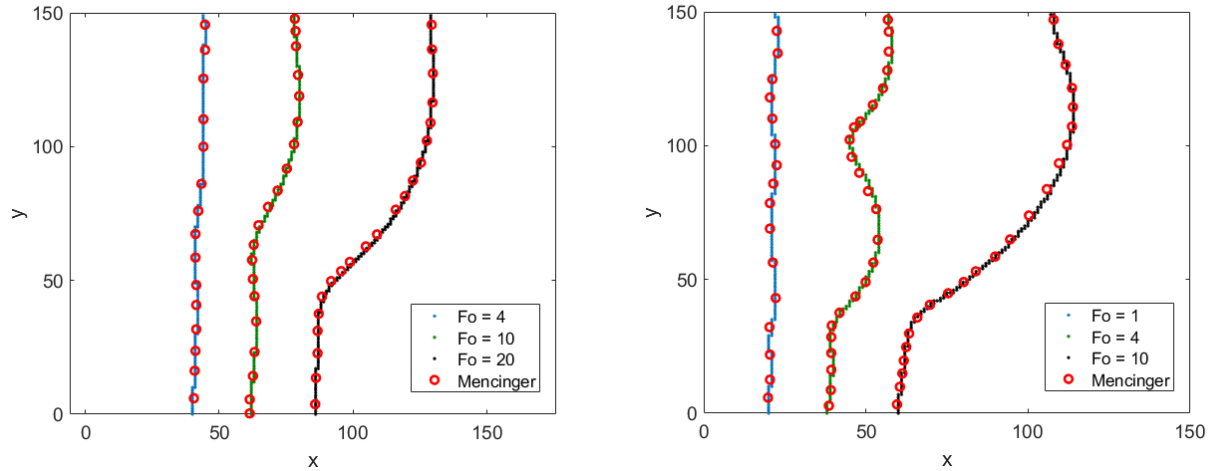

(a) (b)

Figure 6.11 Comparisons between the position of the interface at different Fourier numbers with the simulation results of [3] for (a) Ra = 25000 and (b) Ra = 250000

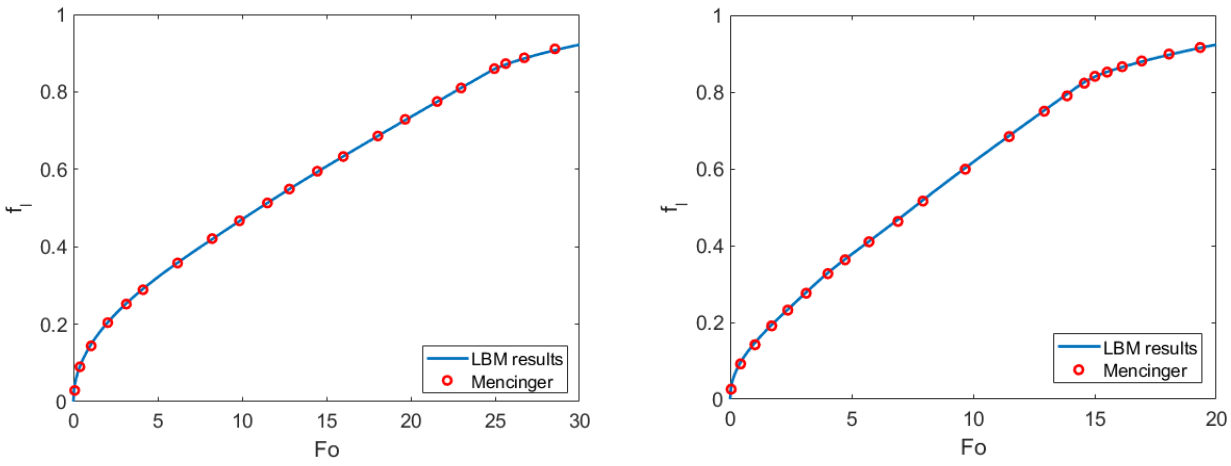

Figure 6.12 Variations of total liquid fraction compared with simulation results of [3] for (a) Ra = 25000 and (b) Ra = 250000

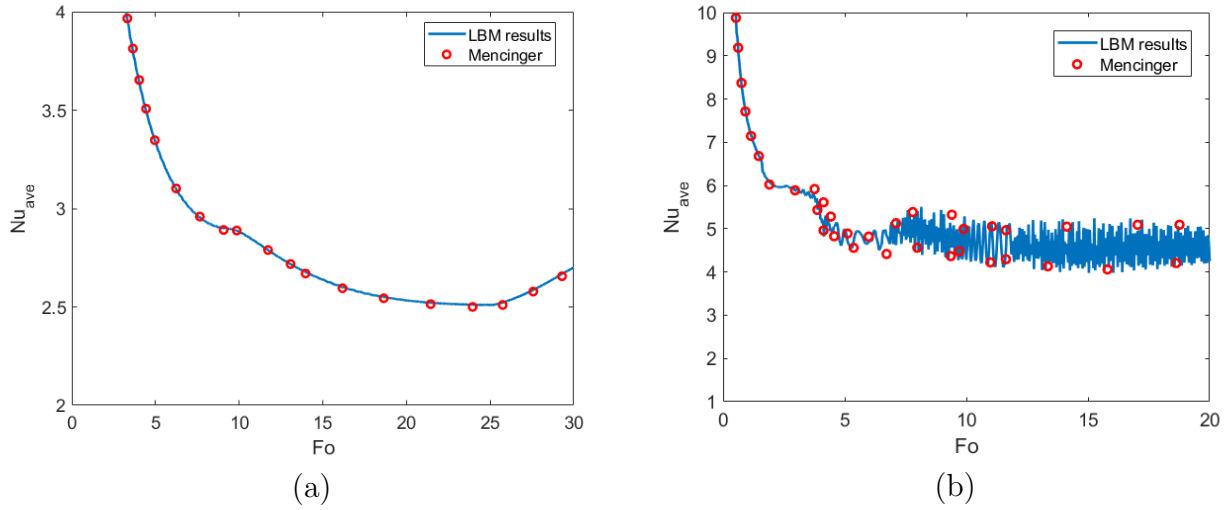

Figure 6.13 Variations of average Nusselt number along the left wall compared with simulation results of [3] for (a) Ra = 25000 and (b) Ra = 250000

CHAPTER 7 LATTICE BOLTZMANN MODEL FOR DROPLET IMPACT AND FREEZING

7.1 Introduction

Water droplet impact and freezing is a transient process with simultaneous heat and mass transfer. This work presents a thermal transport and liquid-solid phase transition based on the pseudo-potential model combined with the enthalpy formation. As it has been already mentioned, the coupled multiphase and total enthalpy method are used to perform the simulation of a droplet impact and freezing.

In this section, we will first present the treatment of the boundaries necessary to simulate the interactions of the droplet with a cold surface. That is the modeling of the contact angle through the application of a force in the pseudopotential model at the fluid nodes next to the solid ones, and the implementation of the fixed Dirichlet temperature at the solid surface. These boundary treatments will be generalized for curved surfaces.

Secondly, we will describe the set up of the test cases and the description of the coupled models in terms of the limitations of the model and the choice of parameters.

Finally, the results and analyses for different test cases will be presented.

7.2 Interaction force for modeling static contact angle

In the pseudo-potential model, the interaction force between the fluid and the solid wall is introduced by the following expression :

$$\mathbf{F}_s = -G_s\varphi(\mathbf{x})\sum_{\mathbf{x}'}\omega(\mathbf{x},\mathbf{x}')s(\mathbf{x}+\mathbf{e}_i)\mathbf{e}_i \tag{7.1}$$

where G_s is the interactive strength coefficient between the fluid and the solid and $s(\mathbf{x}+\mathbf{e}_i)$ is the indicator function of the solid phase with $s(\mathbf{x}+\mathbf{e}_i)=1$ for the wall and $s(\mathbf{x}+\mathbf{e}_i)=0$ for the fluid. The effective mass φ and the weighting factor ω have already been defined. The interaction strength between the fluid and the wall, and therefore the contact angle, can be adjusted by the parameter G_s. It should be noted that this formulation is suitable to allow the modeling of the interaction force on curved surfaces.

Some previous literature suggested that G_s should be negative for all contact angles, representing an attractive force towards the solid, while other studies proposed that G_s should be positive for nonwetting fluid, and negative for wetting fluids. In this case, a zero value of the fluid-wall interaction coefficient, G_s, will produce a contact angle of $\theta = 90°$.

The choice of using one method or another depends on the treatment of the gradient calculation for the fluid-fluid interaction of the pseudo-potential model given by Eq. (4.4). The gradient calculated at the fluid nodes next to the solid ones needs to use these solid nodes to calculate the gradient. If no additional treatment is applied at these points, with the gradient of the effective mass calculated with the values of fictive effective mass from the densities of the solid nodes, only negative values of G_s can be used for the simulation of the interaction of a water droplet on a surface. In this case, $G_s = 0$ will provide a contact angle of $\theta = 180°$ and the droplet will not touch the surface. However this method has a weakness, because for high values of contact angles, there is a smooth interface between the wall and the droplet which does not represent the reality properly.

In this regard, a modification of the gradient of effective mass for the fluid at the boundary nodes has been proposed to be able to use positive values of G_s for nonwetting fluid (contact angles greater than 90°) and negative values for wetting fluid (contact angles less than 90°).

The proposed solution is based on the paper of Leclaire et al. [50] for the prediction step of the calculation of the gradient at the boundary nodes. With this model, the effective mass values calculated at the solid nodes S next to the fluid nodes F are extrapolated using the fluid nodes with a lattice link weighted average as illustrated in Fig. (7.1).

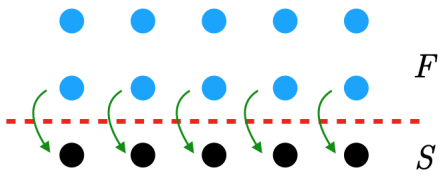

Figure 7.1 Schematic of fluid nodes (F) in blue colour and solid nodes (S) in black colour for the extrapolation from F next to S

$$\varphi(\mathbf{x}_s) = \sum_i \omega_i^s(\mathbf{x}_s)\varphi(\mathbf{x}_s + \mathbf{e}_i\Delta t) \tag{7.2}$$

where $\omega_i^s(\mathbf{x}_s)$ is a directional weight calculated depending on the lattice stencil connections between the fluid and the solid nodes. It is expressed as follows :

$$\omega_i^s = \begin{cases} \dfrac{\omega_i}{\omega_{total}^s(\mathbf{x}_s)} & \mathbf{x}_s + \mathbf{e}_i \Delta t \in F \\ 0 & \text{otherwise} \end{cases} \tag{7.3}$$

$$\omega_{total}^s(\mathbf{x}_s) = \sum_{\{i:\mathbf{x}_s+\mathbf{e}_i\Delta t\} \in F} \omega_i \tag{7.4}$$

This formulation is general for curved interfaces and its benefits are listed below.

1. A better representation of the droplet contact interface with the solid wall. As shown in Fig. (7.2), the simulation of the droplet interaction with the wall represents better the physics of the problem with the extrapolation method (right) than the one without gradient modification (left). We can observe a smooth interface for the density field at the contact of the droplet with the wall that is not found in reality at the length scale of the droplet diameter.

2. A different relationship between the interaction force coefficient and the contact angle. The modification of the gradient force allows representing different wetting and nonwetting contact angles by changing the sign of the interaction coefficient G_s as we can see in Fig. (7.3). Even if the range of contact angles that we can get without the extrapolation is larger than the one with the extrapolation, we still privilege the last one due to its closeness to reality. In the same figure, we can also verify the linear relationship between the interaction force coefficient and the contact angle observed in previous literature.

3. A reduction of spurious currents which appear when applying the immersed boundary scheme for the coupled methods. This influence will be presented when coupling the pseudopotential and the thermal model for phase change in Section 7.5.1.

Therefore, the extrapolation of the effective mass will be applied in all our simulations. Its capability to simulate different contact angles is illustrated in Fig. (7.4). This shows in 2D the steady state from an initial half droplet circle over the surface, for which the interaction force parameter is modified to represent different contact angles. Gravity is not considered. The contact angle is calculated according to appendix A.

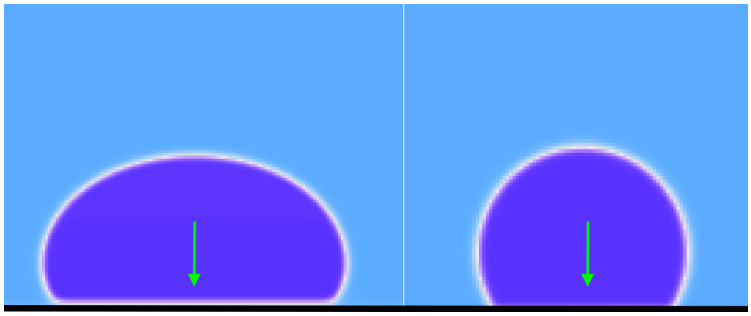

Figure 7.2 Density field for the droplet interaction with a wall for two treatments at the interface : without extrapolation (left) and with extrapolation (right)

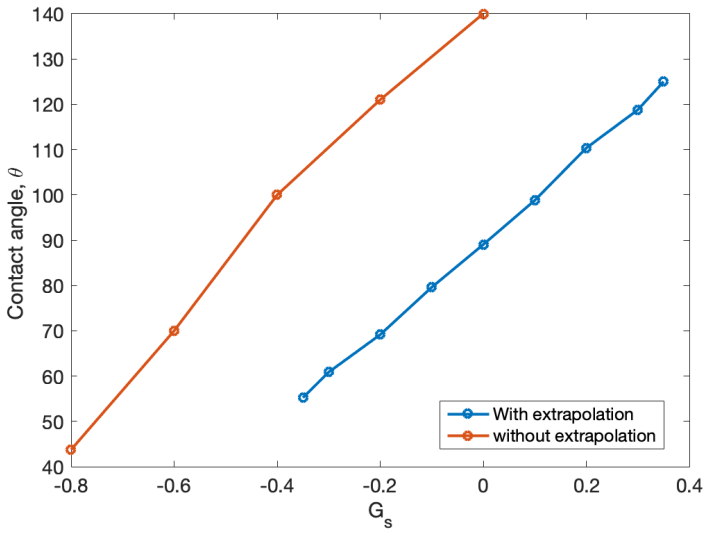

Figure 7.3 Contact angle against interaction strength

7.3 Temperature Dirichlet boundary condition at curved wall

The droplet impact on a cold surface provides a nucleation point to start the freezing process. As it can be considered that the surface remains at a constant temperature, during the solidification, a Dirichlet boundary condition will be applied to the solid nodes.

The Dirichlet boundary condition for the temperature at a curved surface can be easily applied following the approach proposed by M. Yoshino and Inamuro [51] for a fixed concentration on a body. We can apply this condition for temperature as we are solving the same convection-diffusion equation.

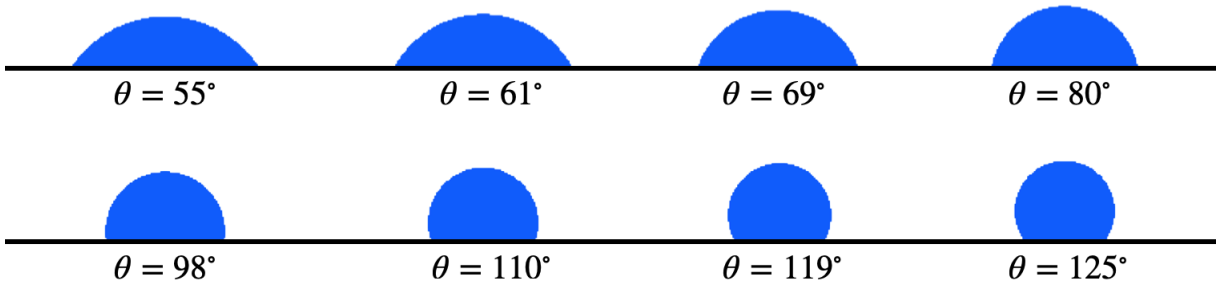

Figure 7.4 Simulated contact angles for multiphase fluid interacting with a surface

The interface between the fluid and the solid is considered by means of $\mathbf{n}$, which is the normal vector at the interface towards the fluid. For a fluid node next to solid nodes, the populations of the thermal distribution function at that node, such that $\mathbf{e}_i \cdot \mathbf{n} > 0$, are unknown. For a fixed temperature value at the boundary, the unknown distributions are assumed to be represented through the equilibrium distribution functions with an unknown temperature T_σ :

$$g_i = \omega_i T_\sigma \quad \mathbf{e}_i \cdot \mathbf{n} > 0 \tag{7.5}$$

Where the parameter T_σ is calculated so that the temperature at the boundary node is given by the fixed value T_w and is determined as follows :

$$T_\sigma = \frac{T_w - \sum\limits_{\{i:\vec{c}_i \cdot \vec{n} \leq 0\}} g_i}{\sum\limits_{\{i:\vec{c}_i \cdot \vec{n} > 0\}} \omega_i} \tag{7.6}$$

7.4 Coupled models

Now that all the required elements have been presented, we can build a model for simulating a droplet impact and freezing. However, it is important to mention that the simulation strategy has some limitations.

In section 6.4.1, we validated the coupled thermal and fluid fields with a double-distribution function approach and the use of an immersed boundary scheme (IBS) for the nonslip velocity at the interface. The performed test was the natural convection with phase change. In order to include a droplet, we need to add the pseudo-potential interaction forces to the fluid particle distribution functions. That is the fluid-fluid interaction from Eq. (4.3) and the interaction force with the surface described in the previous section. Regarding the thermal model, instead of using the simple LB equation for the temperature field, we will use the

total enthalpy model (Chapter 6) which allows the phase change. The thermal model will be applied to all the nodes but we only want the phase change to happen for the liquid phase. In order to achieve this, the liquid-gas interface must be defined. We use the intermediate density ρ_m between both phases to establish this interface. This is an assumption concerning the position of the interface with our diffuse interface model.

In the application of IBS, we need to set a solid velocity once a liquid node becomes solid. As we do not model the fluid-structure interaction between the fluid and the ice, we will set this velocity to zero. This is a reasonable consideration because the contact with the surface is the reason for nucleation, and the wall is stationary. With this approach, a liquid node that turns into ice will keep its position so that we can only consider solidification when the droplet contacts the surface.

Another consequence of this is that we need to initialize the temperature field after the contact of the droplet with the surface. We are also considering the conduction of the thermal field in the gas and if the melting temperature is achieved before the droplet contacts the surface, it will wrongly freeze in the air and stay at this position (as per our assumption of not modeling the fluid-structure interaction and set velocity to zero) while the liquid part will still be falling.

Regarding the fluid thermal properties, we saw how we can consider different thermal capacities and diffusivities for solid and fluid phases with the total enthalpy model. However, we are not making any difference between gas and liquid thermal properties.

When the coupling was presented, we included the Boussinesq term that accounts for the natural convection, but for the following tests, this phenomenon can be neglected and this forcing term will be omitted.

In order to clarify all the considered phases and interactions between them, figure 7.5 shows all the phases displayed in our simulations. The condition for each phase is :

1. gas : $\rho < \rho_m$ and $f_l = 1$
2. liquid : $\rho > \rho_m$ and $f_l = 1$
3. ice : $f_l = 0$
4. mushy zone : $0 < f_l < 1$

5. solid : predetermined for setting the boundaries

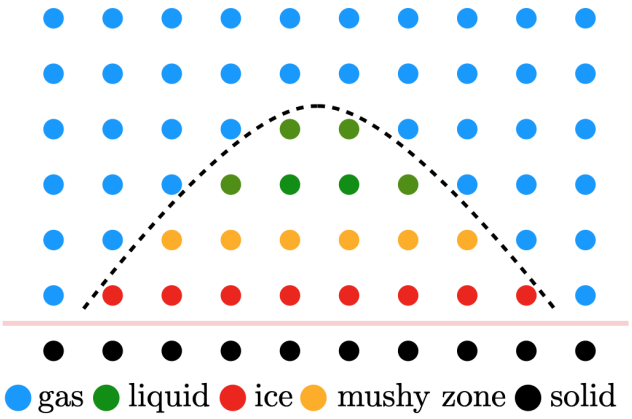

Figure 7.5 Interactions and forces applied to the different possible nodes in the simulation domain

Regarding the different interactions between these phases and the different conditions applied, we have :

1. FFI : fluid-fluid interaction from the pseudo-potential model Eq. (4.3)
2. FSI : fluid-solid interaction to model the contact angle Eq. (7.1)
3. EXT : Extrapolation of the gradient of the fluid-fluid interaction Eq.(7.2)
4. IMB : Immersed boundary condition : modified collision (MC) Eq. (6.24) or anti-bounce-back of non-equilibrium part (NE) Eq. (6.28)

These interactions are applied according to table 7.1. On the one hand, diagonal cells represent the interactions between the same phase or the conditions applied at the same phase. On the other hand, non-diagonal cells show the interactions between different phases and blank cells indicate that the interaction is not modeled.

7.5 Simulation results and discussion

To evaluate the performance of the coupled model developed in the previous sections, we have carried out numerical simulations for droplet impact and freezing under different conditions and geometries.

Table 7.1 Interactions between phases

Phase	liquid	gas	ice	solid	mushy zone
liquid	FFI	FFI		FSI/EXT	
gas	FFI	FFI		FSI/EXT	
ice			IBM-NE		
solid	FSI/EXT	FSI/EXT			
mushy zone					IBM-MC

Firstly, we will perform the solidification of a static droplet on a cold flat plate. For this test, we will evaluate the influences of the contact angle, Stefan number, and droplet size on the solidification process. A three-dimensional implementation will be used to validate our model by comparing results with experimental and numerical data found in the literature.

Secondly, we will perform the impact and freezing of water droplets on a cold flat surface. The influences of the contact angle and Reynolds number will be analyzed.
And finally, we will exploit the adaptability of the model on curved surfaces by simulating the impact and freezing on airfoils.

7.5.1 Droplet solidification on a cold flat plate

The first test concerns the solidification of the droplet on a cold flat plate. In the initial state, the droplet is in a liquid state at the center of the domain and there is no solid phase region. The temperature of the domain is higher than that of the cold flat plate and freezing point. In this model, we do not consider the supercooled state of the droplet as the droplet is initially at a higher temperature than the freezing point. Besides, the effect of recalescence (liberation of the latent heat necessary to be at the freezing point and allow the phase change) can be neglected in the solidification process [16]. For the velocity field, non-slip boundary conditions are applied through the full-way bounce-back for the distribution functions on the top and bottom walls. Periodic boundary conditions are used between the left and right sides. For the temperature, periodic boundary conditions are also applied along the sides. Dirichlet boundary conditions are enforced at the bottom cold wall and for the warm temperature on the top.

For this test, we initialize the fluid domain and let the droplet impact the surface under isothermal conditions. There is an initial stage where a droplet deformation period is observed before it finally reaches an equilibrium position due to the balance of surface tension, viscous forces, and gravity. Once there is no more deformation on the droplet (a determined simulation time t_{eq} depending on mesh and Reynolds number Re), the thermal field

is activated and solidification of the liquid phase starts. The boundary conditions and the computational domain for the initial configuration and the thermal boundaries are shown in Fig. (7.6). The initial conditions for the fluid field with the aforementioned boundary conditions are shown in the left of Fig. (7.6). When the droplet reaches an equilibrium contact angle at t_{eq}, the thermal equation is activated and the Dirichlet BC showed in the right of Fig. (7.6) are applied. The temperature at the surface is lower than the freezing temperature $T_w < T_f$ and the temperature on the top boundary is higher than the freezing temperature $T_{air} > T_f$. This temperature will be the initial temperature of all the domain expect from the cold surface.

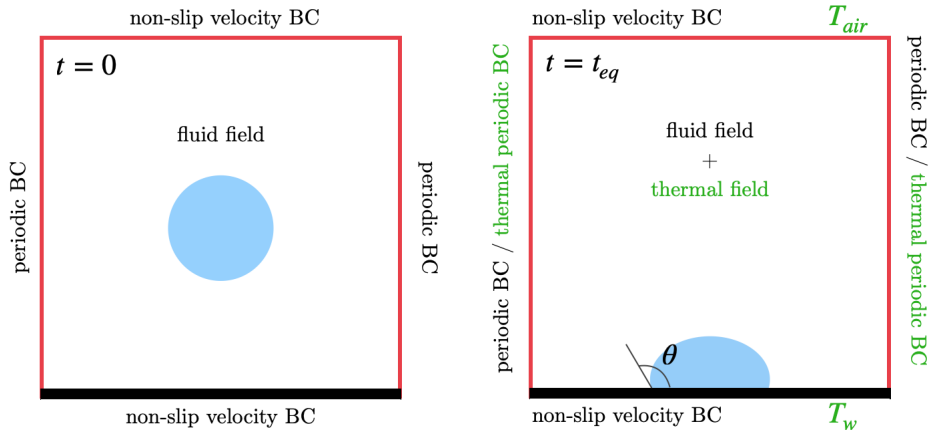

Figure 7.6 Boundary conditions and initial state for the isothermal falling droplet (left) and for the temperature field activation at time $t = t_{eq}$ (right)

The simulation results are presented in terms of dimensionless numbers. The initial diameter of the droplet D is chosen to be the characteristic length. The dimensionless time and velocity are embedded in the Fourier number and Reynolds numbers respectively, while the Stefan number controls the speed of solidification. These dimensionless numbers are defined as :

$$\mathrm{Re} = \frac{uD}{\nu}, \quad \mathrm{Fo} = \frac{\alpha t}{D^2}, \quad \mathrm{Ste} = \frac{C_p(T_f - T_w)}{L_{ls}} \tag{7.7}$$

where u is the impact velocity, ν is the kinematic viscosity, α is the thermal diffusivity, C_p is the liquid heat capacity, T_f is the freezing temperature, T_w the wall temperature and L_{ls} is the latent heat of phase change.

Qualitative validation of three dimensional model for static droplet solidification on a plate

To validate the proposed model, the simulation results of this test are compared with experimental results from literature. For that, a 3D implementation of the model is used (Appendix B).

The computational domain is a grid of $100 \times 100 \times 100$ in lattice units (lu). The droplet has a radius of 16 lu with the center initially at $x = 49.5$, $y = 49.5$ and $z = 25.5$. The droplet is moving downward with a Reynolds number of Re = 15. For the simulations, we choose a reduced temperature of $T_r = 0.8$ which gives a density ratio of approximately 85 between phases. This density ratio will be used for all the simulations of this work. The freezing temperature is set to $T_f = 0$ and the wall temperature to $T_w = -1$ (in lu). The initial temperature is the same as the fixed temperature on the top which is set to $T_i = T_{air} = 0.3$. For the thermal properties of fluid and solid, $C_{pl} = 1$, $\lambda_l = 1/6$, $R_{C_p} = 0.5$ and $R_\lambda = 1$. The Stefan number is set to Ste = 2 and the thermal equation is activated at $t_{eq} = 4000$ time steps, when the oscillation of the droplet is finished.

Figure (7.7) shows a comparison of the water droplet evolution between our simulation results and photographs from the experimental results of [4]. We represented the same contact angle of $\theta = 79°$ and a qualitative comparison of the evolution of the solidification front is shown. In the simulation results, white and blue colors represent solid and liquid phases, respectively. We can observe how the concave interface is well displayed in the simulation results, and also the volume expansion of the droplet as a result of the density ratio between the liquid and the solid. This effect is more noticeable at the final stage where the top of the droplet deforms and a singular tip appears. As observed in [4], the volume expansion is slight in the early stage. It should be pointed out that the time scales are not the same between simulation and experimental results, because we are not considering the same thermal diffusivity and no dimensionless time parameters are analyzed. Besides, the tip deformation observed in experience is sharper than the one found in the simulation.

The same configuration is used to analyze the temperature field of the domain and determine if it agrees with what was expected. Fig. (7.8) depicts the snapshots of the temperature field (7.8a) and the evolution of the temperature along z-axis above the center of the cold surface (7.8b) for four different Fourier numbers. These time steps represent the initial configuration, the start of the freezing, some intermediate point, and the end of the freezing. We can observe how the conduction of the temperature is modified by the presence of the droplet

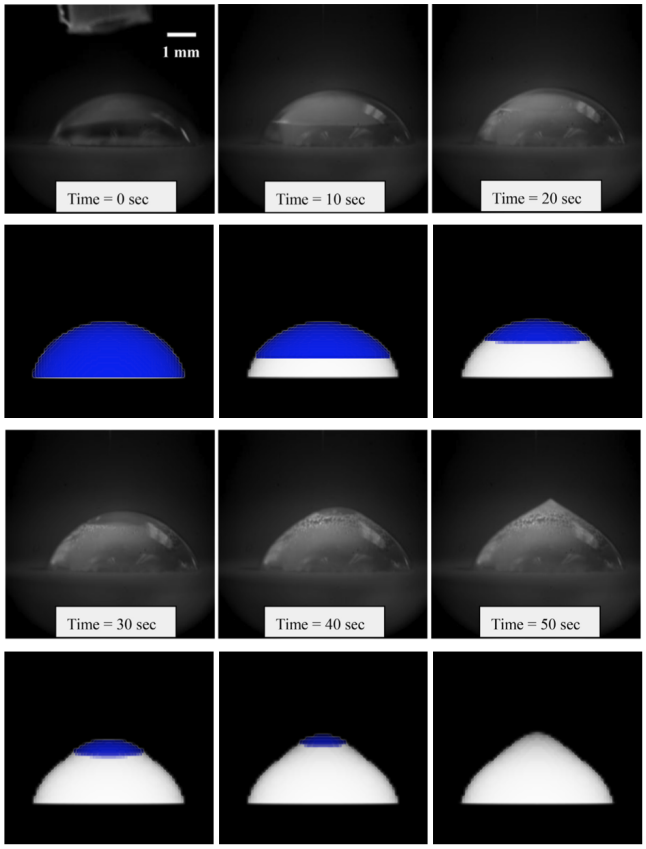

Figure 7.7 Comparisons of water droplet evolution on a cold flat plate between simulations and snapshots of the time-sequential images from [4]

and its freezing. For Fo = 0.09 in Fig. (7.8b), we can see a slight change of the slope at the liquid-solid interface (at the freezing temperature $T_f = 0$) due to the change of the thermal conductivity. Following this, there is a remarkable increase in the temperature because of the liberation of the latent heat. Finally, the temperature reaches the ambient constant value. It should be mentioned that the same trend was observed by Jianan et al. [30] in their LB model for the solidification of water droplets. We do not use their results to compare as their model and set up of the test is different. They consider a cryogenic spot at the surface, instead of all the bottom surface at the same temperature, and the model and simulation parameters are also different.

We use the same test to illustrate the other advantage of using the extrapolation of the gradient at the surface as explained in Section 7.2. We mentioned that the application of immersed boundary method delivered some spurious currents at the surface when no extrapolation was applied. As the equilibrium function of the thermal field depends on velocity,

the spurious currents can modify the representation of temperature variations. Figure (7.9) shows the temperature variation at the same time step along z-axis at the center of the domain with and without the extrapolation applied. We notice how without the extrapolation there is a decrease of the temperature near the surface under the value of the surface temperature which does not make sense as there is no other source of heat transferred to the droplet.

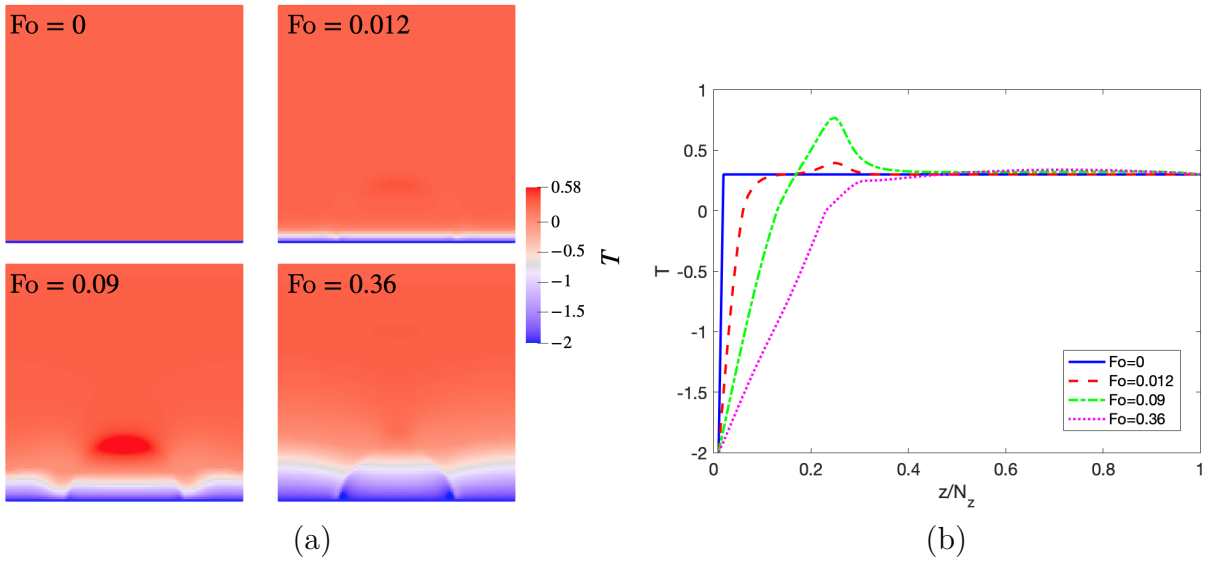

(a) (b)

Figure 7.8 Snapshots of the temperature field (a) and temperature along z-axis above the center of the cold plate (b) for four different Fourier numbers

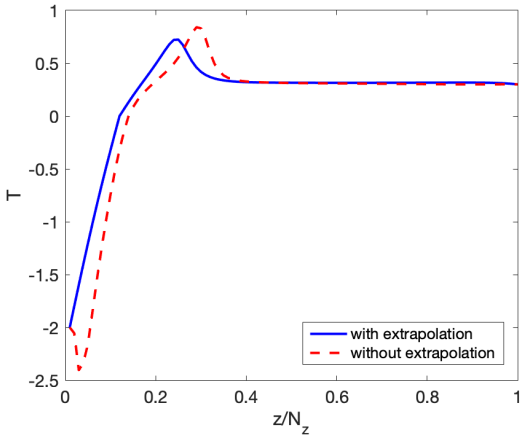

Figure 7.9 Temperature evolution along the z-axis above the center of the cold plate with and without the extrapolation of the gradient at the surface

As a final test, we compare our simulation results with the results from Chaudhary et al. [5] for the evolution of the solid front. We simulated the same contact angles that they performed in their simulation and experimental tests and we calculated the dimensionless Fourier number for their physical data. A comparison between their results and our simulation results are shown in Fig. (7.10). We can see that trends for different contact angles are similar to the ones found in the literature. However, there is a discrepancy in terms of time scales for the final freezing time. There are many potential sources for this discrepancy because we may not calculate the same dimensionless parameters in the same way and there are also many other parameters that cannot be equal to the reference as the fluid properties, the real freezing conditions and time scales, among others.

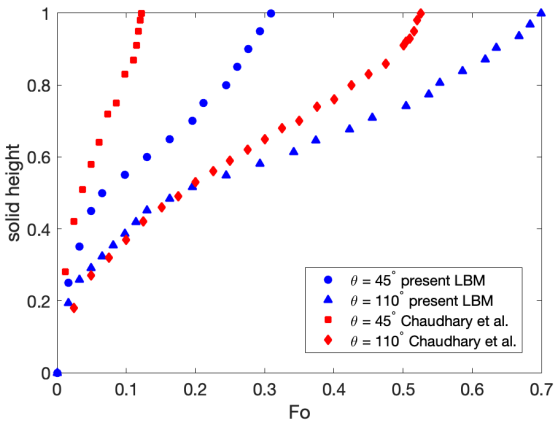

Figure 7.10 Comparisons of the solid height evolution normalized by the droplet center height with numerical results from [5]

Effects of surface wettability

As it has been shown in the previous subsection, the proposed model provides simulation results which seem to agree qualitatively with experimental data and simulation results. We will now study the influence of different parameters on the solidification process. The effects of the contact angle, Stefan number, and droplet size will be analyzed. For that, a 2D implementation will be used to reduce simulation time and increase the number of nodes used in the domain for a refined grid.

The computational domain is a space of 200×200 in lattice units. The droplet has a radious of 22 lu with the center at $x = 99.5$ and $y = 25.5$. The same droplet density ratio of the 3D simulation is used. Regarding the thermodynamic properties, the following param-

eters are used: $C_{pl} = 1$, $\lambda_l = 1/6$, $R_{C_p} = 0.5$ and $R_\lambda = 1$. For the temperatures: $T_w = -2$ and $T_i = T_{air} = 0.3$. These parameters will remain the same unless specifically indicated otherwise.

In order to investigate the effects of the contact angle on the static droplet freezing, different contact angle surfaces are simulated ($\theta = 61°$, $\theta = 75°$, $\theta = 90°$, $\theta = 104°$ and $\theta = 119°$) with the same Stefan number of Ste = 2. Figure (7.11) shows the snapshots of LB simulated results for the different contact angles at three different dimensionless times: before the freezing process starts, at some point in the middle of the process and the final time of droplet freezing for the larger contact angle. The droplet is indicated in dark blue color and the formation of ice in light blue. The wall is represented by a black line. It is shown that for the intermediate dimensionless time, the smaller the contact angle, the more advanced the solidification front is. We can observe that when the case of higher contact angle freezes, smaller cases have also finished the process.

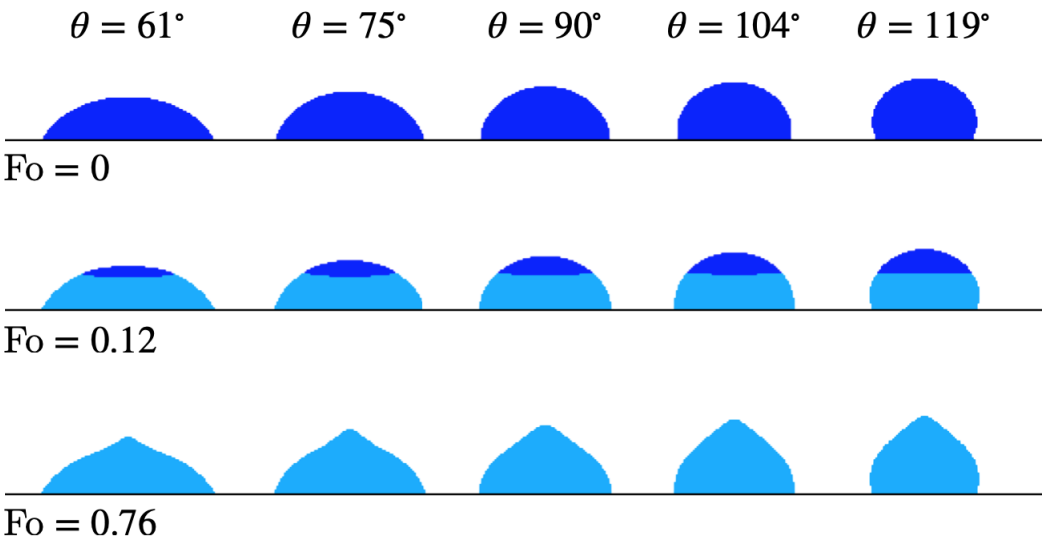

Figure 7.11 Snapshots of different contact angles θ of droplet freezing on a wall at three different dimensionless times Fo

Figure (7.12) shows the temporal variation of the total solid fraction (7.12a) and the evolution of the solidification front normalized by the frozen droplet center height (7.12b) against Fourier number for the same different contact angles. The total solid fraction is defined as the number of nodes in solid phase divided by the total number of ice phase nodes at the

end of the simulation as shown in Eq. (7.8).

$$\text{total solid fraction } (t) = \frac{\sum_i (1 - f_{li}(t))}{\sum_i (1 - f_{li}(t_f))} \tag{7.8}$$

For its temporal evolution, we can see how the freezing time is increased with the contact angle. This is expected and is because the contact area between the droplet and the cold surface is smaller for greater contact angles, which leads to a fewer heat released from the droplet and therefore a longer freezing time. So, the surface with a larger contact angle can delay the solidification process. It can be seen that the increasing rate of the solid fraction is slower at the final stage than that in the beginning. This was also observed by Sun et al. [7]. Regarding the evolution of the interface, it can be noticed that the displacement speed of the solid front changes over time and exhibits different trends. There is an accelerated process at the start and the end of the solidification process.

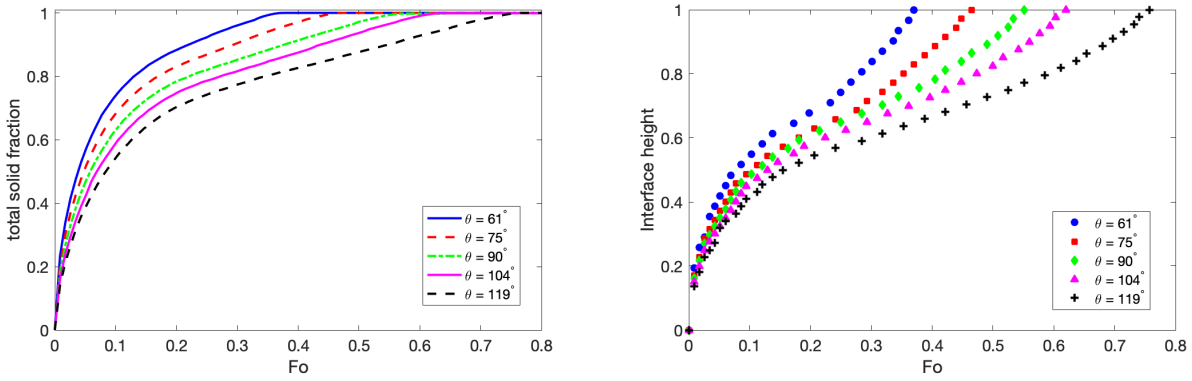

(a) (b)

Figure 7.12 Effects of contact angle θ on temporal variations of total solid fraction (a) and interface height (b) normalized by frozen droplet center height

The total dimensionless freezing time ($\text{Fo}_f = \alpha t_f / D^2$) against the contact angle is illustrated in Fig. (7.13), which shows that the freezing time increases linearly with the contact angle which was also observed in [52], for the range of contact angle simulated. For greater contact angles, the freezing time increases faster as the contact area is reduced.

Effects of Stefan number

We will now analyze the effects of the Stefan number on the solidification process. The Stefan number controls the solidification speed as it is the ratio of sensible heat to latent heat. For

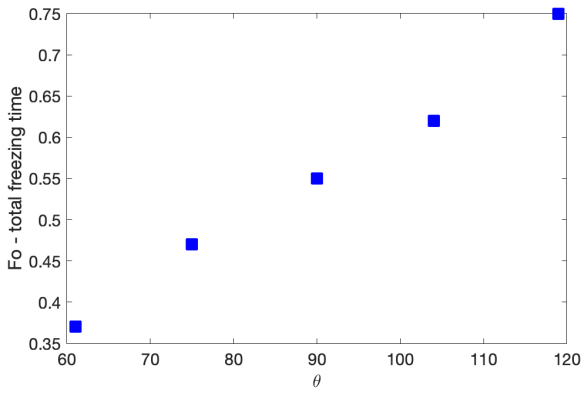

Figure 7.13 Variations of total droplet freezing time with different contact angles

the same fluid, an increase of the Stefan number means a lower surface temperature. This characteristic will be helpful for studying the influence of changing the wall temperature on the freezing process.

For the same computational domain of the previous test, we will now fix the contact angle at $\theta = 90°$ and sweep in Ste number. Snapshots of the LB simulated results at the same dimensionless time for several Stefan numbers (Ste = 0.8, Ste = 1.6, Ste = 3.2, Ste = 6.4) are illustrated in Figure (7.14). We can see how an increase of Stefan number provides a more advanced solidification front. Fig. (7.15) depicts the temporal variation of the total solid fraction (7.15a) and the evolution of the solidification front normalized by the frozen droplet center height (7.15b) against the Fourier number for different Ste numbers. The evolution of the solid fraction shows a faster freezing process at an early stage and a lower solidification rate near the end of the process. This is because the growing ice beads will produce a higher thermal resistance which slows down the freezing. These effects are also noticeable in the evolution of the solid height over time.

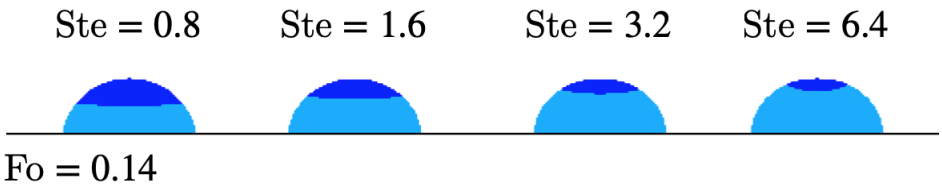

Figure 7.14 Snapshots of different Stefan numbers of droplet freezing on a wall at the same dimensionless time (Fo = 0.14)

Finally, Fig. (7.16) depicts the total freezing time against Stefan number. Total freezing

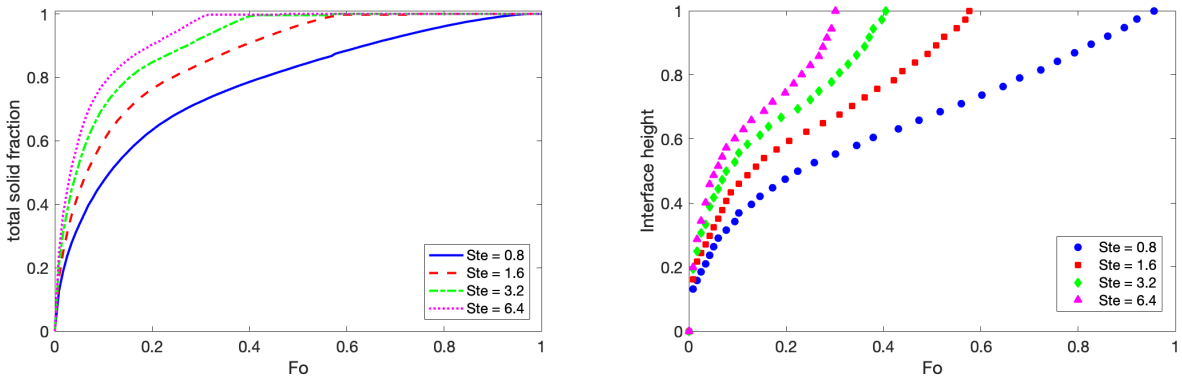

(a) (b)

Figure 7.15 Effects of Stefan number on temporal variations of total solid fraction (a) and interface height (b) normalized by frozen droplet center height

time decreases rapidly with the increase of Stefan number and the evolution seems to be exponential. This reveals the great influence of wall temperature on the freezing process of static water droplets.

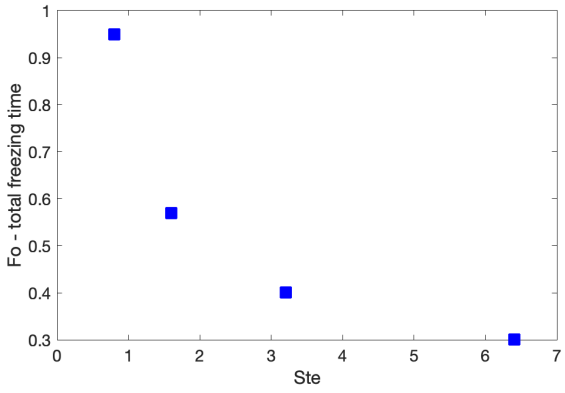

Figure 7.16 Variations of total droplet freezing time with different Stefan numbers

Effects of droplet diameter

For the intended application of icing on UAVs, all the droplets do not have the same diameter. For this reason, we will analyze the influence of changing the droplet size on the freezing time.

Figure (7.17) depicts the snapshots of four different droplet diameters before and after freezing for the same contact angle of $\theta = 90°$ and Stefan number of Ste $= 2$. As shown, the shape of the frozen droplet is almost similar for all the diameters. Regarding the freezing

time, Fig. (7.18) shows a linear evolution of the total freezing time with droplet diameter. The larger the droplet diameter, the longer the freezing time.

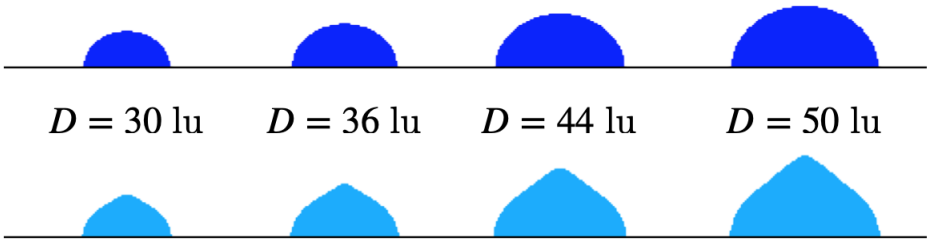

Figure 7.17 Snapshots of different droplet diameters of droplet freezing on a wall before and after freezing

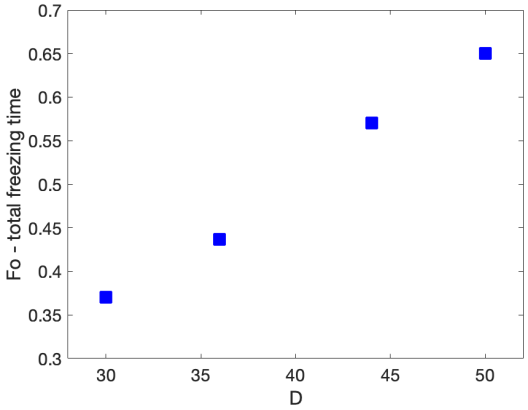

Figure 7.18 Variations of total droplet freezing time with droplet diameter

7.5.2 Droplet impact and freezing

In the previous test case, we studied the freezing of a static droplet over a cold flat plate. We will now analyze the impact and freezing of a droplet over a cold surface. The influences of Reynolds number and contact angle on the freezing time and spreading parameter will be studied in this subsection.

To simulate the impact and freezing with the presented model considering the limitations outlined in section 7.4, the thermal field is activated once the droplet makes contact with the surface. This will lead to the solidification of the droplet once the contact is made because the surface triggers the nucleation process.

For this test case, the same previous (subsection 7.5.1) two-dimensional grid and thermal parameters are used to carry out the simulations unless otherwise mentioned.

Effects of Reynolds number

To analyze the effects of Reynolds number based on the impact velocity, we initialize the droplet at the center of the domain ($x = 99.5$, $y = 99.5$) and we change the gravity value in lattice units through the Reynolds number. For this test, we use a hydrophobic surface with a contact angle of $\theta = 119°$ and four Reynolds numbers (Re = 10, Re = 20, Re = 30 and Re = 40).

Figure (7.19) depicts snapshots of the LB simulations for two Reynolds numbers (Re = 20 and Re = 40) at four different Fourier numbers: initial time, two intermediate instants and the final freezing for Re = 40. We can observe how a higher Re number results in a faster contact of the droplet with the surface and a larger spreading of the droplet on the surface. This faster contact finally produces an anticipated freezing from the lower Re. The variation

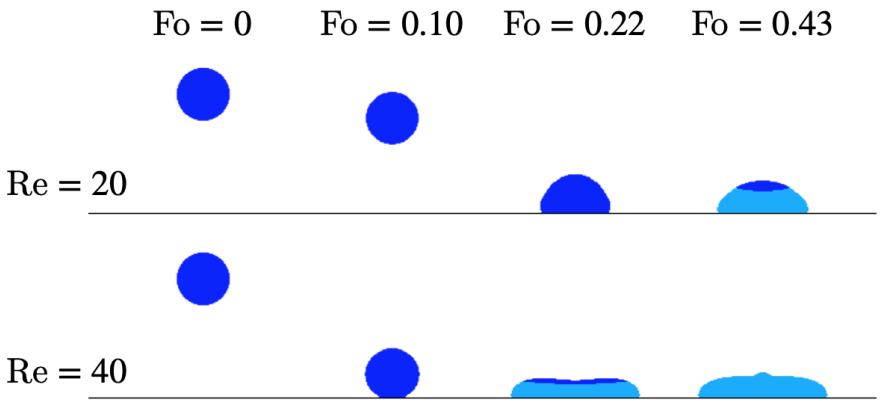

Figure 7.19 Snapshots of different Reynolds numbers for the impact and freezing at four time steps

of the total solid fraction and the normalized solidification front height by the solid center height are presented in Fig.(7.20). The solidification takes longer to start for lower Re numbers as the contact is made later. Regarding the evolution of the solidification front, higher Re delivers an increased freezing rate and trends are more pronounced.

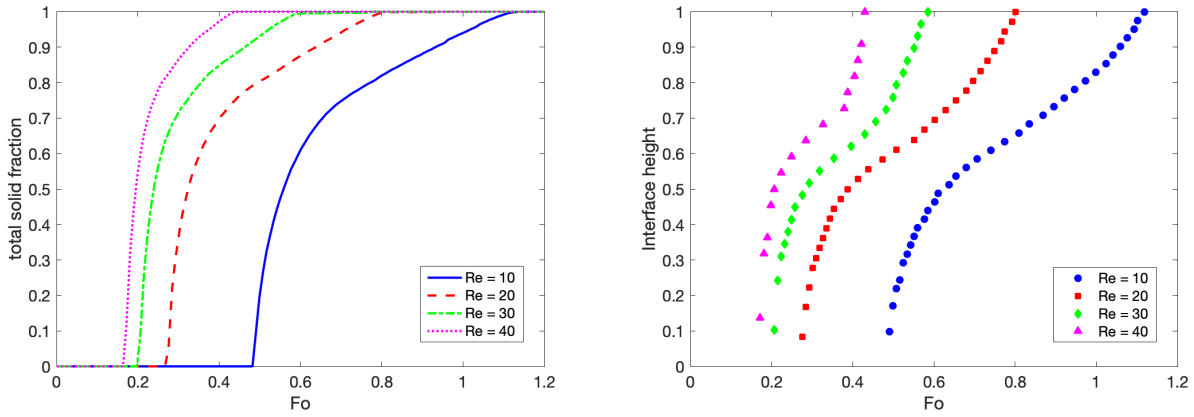

(a) (b)

Figure 7.20 Effects of Reynolds number on temporal variations of total solid fraction (a) and interface height (b) normalized by frozen droplet center height

Finally, Fig. (7.21) shows the total freezing time variation with Re (7.21a) and the temporal evolution of the spreading parameter (7.21b). The freezing time is reduced as Re is increased as a consequence of the augmentation of the contact surface of the droplet with the surface. The spreading parameter is defined as the contact diameter of the droplet on the ice surface divided by the droplet diameter (D/D_0). We can see how the spreading factor increases rapidly up to a maximum value and then remains constant due to the freezing at the contact with the surface. This behavior was also observed by Jin et al. [15] in their experimental results. This maximum spreading factor is increased by the Re number because for higher impact velocities the deformed diameter is larger for droplets with the same volume. This effect can also be observed in Fig. (7.19). The higher is the droplet impact velocity, the easier the freezing occurs.

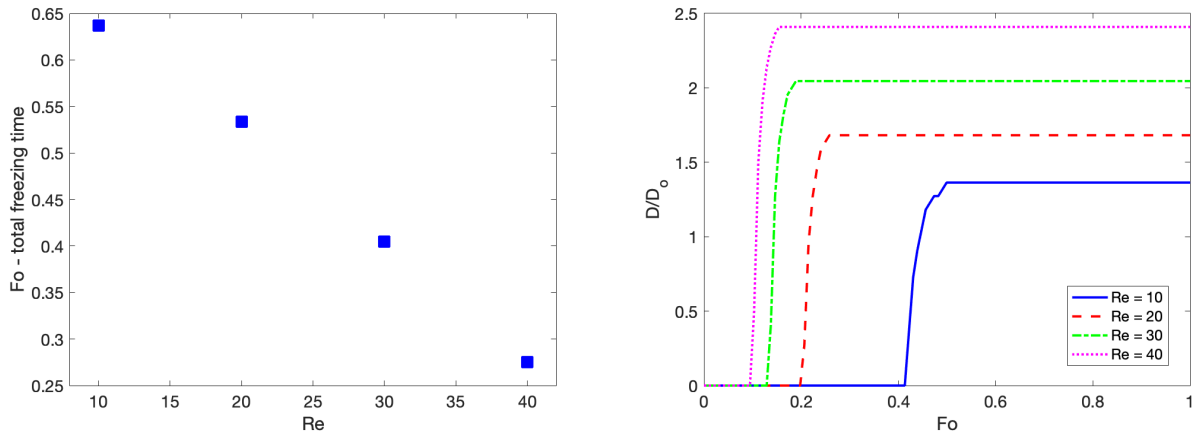

(a) (b)

Figure 7.21 Total freezing time against Reynolds number (a) and temporal variation of spreading factor for different Reynolds numbers (b)

Effects of contact angle

The influence of the contact angle on the static droplet freezing has already been studied. We saw how a larger contact angle means an increased total freezing time because of the smaller area in contact with the surface and the larger droplet height. Now, we will see how the contact angle influences the freezing process when considering the impact on the surface.

To study the freezing process by changing the contact angle, we will use the same configuration used before, but now we will fix the Reynolds number to Re = 20 and Ste = 2, and we will simulate five different contact angles ($\theta = 61°$, $\theta = 75°$, $\theta = 90°$, $\theta = 104°$ and $\theta = 119°$). Figure (7.22) shows the temporal variation of the solid fraction (7.22a) and the spreading factor for several contact angles (7.22b). The total solid fraction seems to have a similar trend found for static droplets, but in this case, the solidification seems to happen faster. We can observe how the larger the contact angle, the longer the freezing time. However, the difference in the evolution of the total solid fraction between the different contact angles is less noticeable than for the static freezing.

For the spreading factor, we found the same trend observed for the Reynolds number variation: the spreading factor increases up to a maximum value and then it remains constant. This corresponds to a simulation of instant freezing when the contact with the surface is made. In reality, depending on the impact and surface conditions, the droplet may reduce

its diameter and freeze with a smaller spreading diameter. Regarding our simulation results, it can be inferred that the lower the contact angle, the larger the spreading diameter. These results are illustrated in Fig. (7.23).

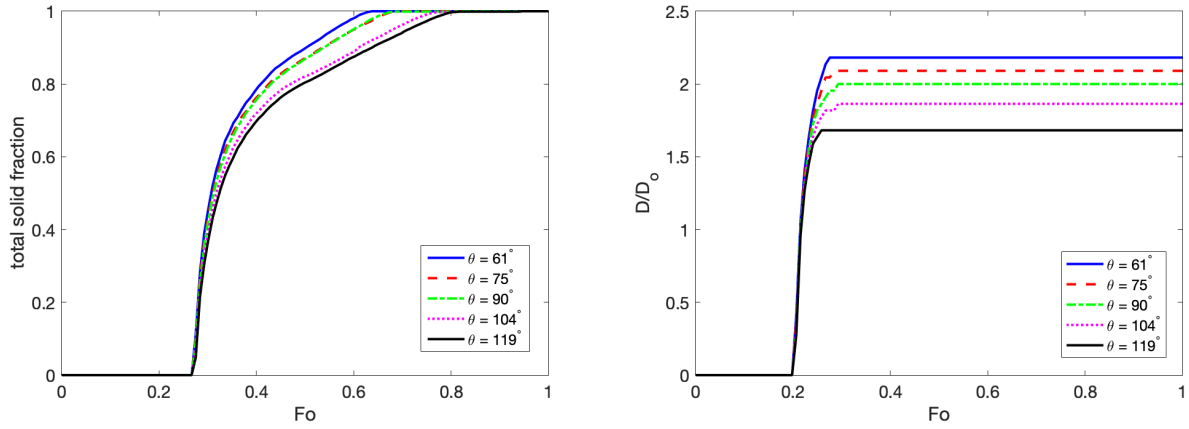

(a) (b)

Figure 7.22 Total freezing time against Reynolds number (a) and temporal variation of spreading factor for different Reynolds numbers (b)

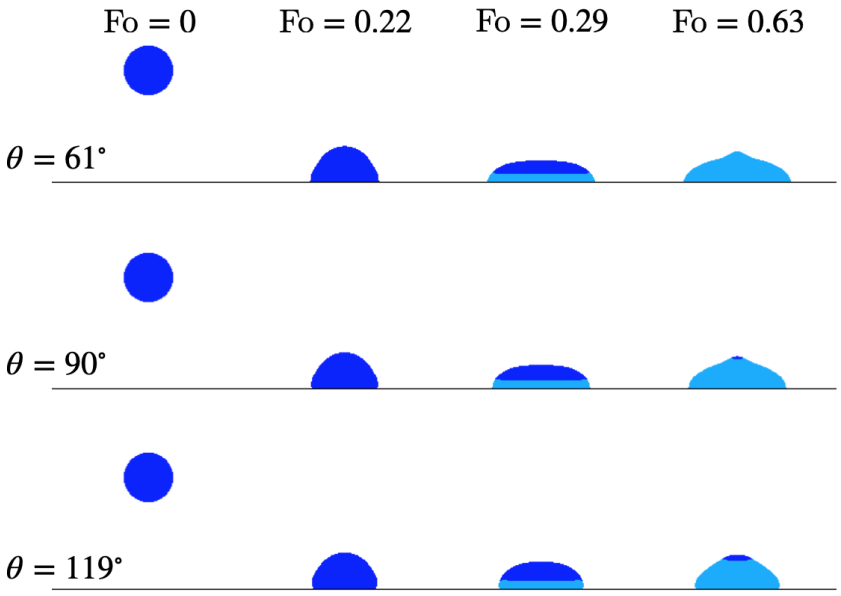

Figure 7.23 Snapshots of different contact angles for droplet impact and freezing at four time steps

7.5.3 Droplet impact on curved surfaces

The intended application of this research project is the study of the ice accretion on drones. This is mainly caused by the impact and freezing of supercooled super large water droplets on the airframe and rotor blades.

As mentioned in the introduction of this section, the proposed model has been coded so that it can perform droplet impact and freezing not only on flat cold surfaces, but it can also simulate the solidification on curved surfaces. For that reason, we carried out the simulation of a water droplet impacting and freezing on a NACA0012 airfoil. The scales used for the droplet size and the airfoil could be found on drones rotors.

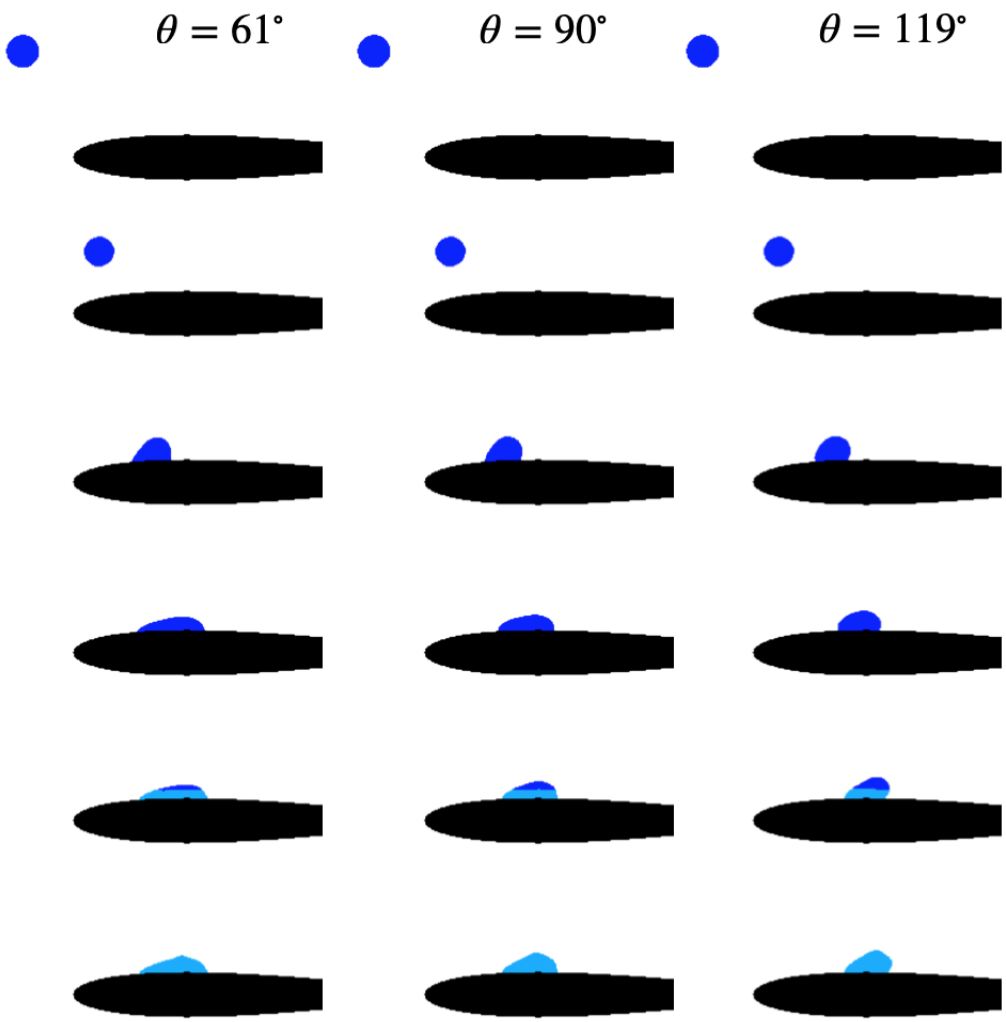

Figure 7.24 Snapshots of a water droplet impact and freezing on a NACA0012 airfoil for three different contact angles at different time steps, Re = 50, and Ste = 2

Figure (7.24) depicts the snapshots of the simulated water droplet impacting on an airfoil for three different contact angles ($\theta = 61°$ [hydrophilic], $\theta = 90°$ and $\theta = 119°$ [hydrophobic]) at different time steps. We can observe how a smaller contact angle results in a larger contact area with the surface and therefore faster freezing. For the hydrophobic surface, there is a runoff of the droplet before it starts freezing. It should be mentioned here that we are not considering a steady airflow in our simulation. This could provide the droplet another source for leaving the airfoil before freezing starts. This highlights the capability of the hydrophobic surfaces to delay the freezing or even to avoid it.

Finally, we outline the capability of the proposed model to perform the simulation of the impact and freezing of several droplets at the same. The simulation results are presented in Fig. (7.25) where we simulated three droplets impacting a surface with a contact angle of $\theta = 90°$.

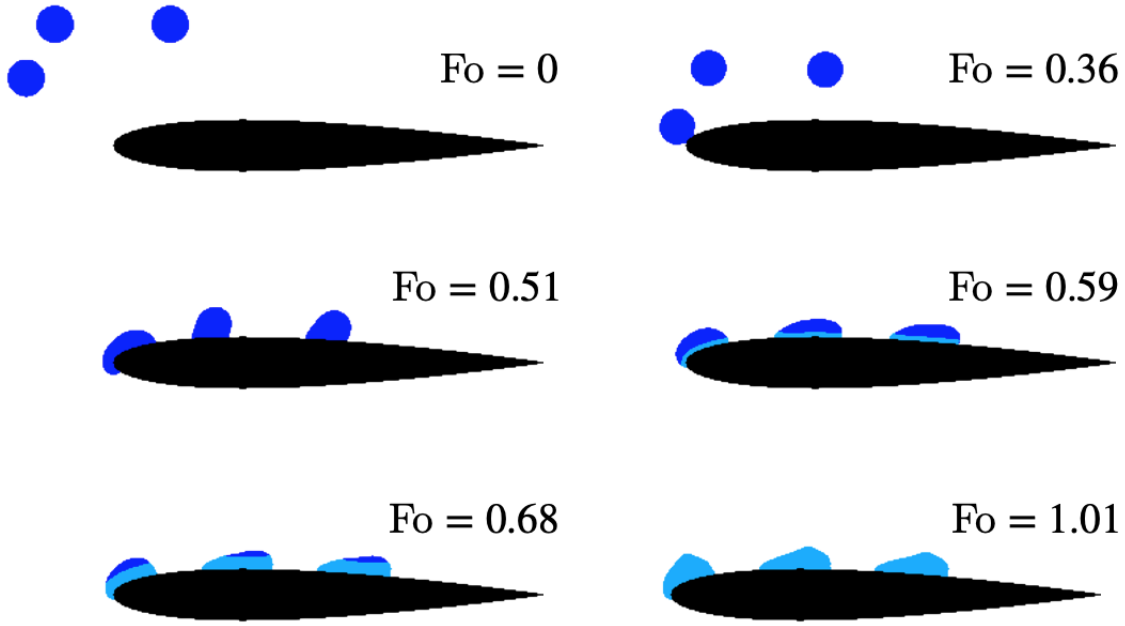

Figure 7.25 Snapshots of three water droplets impact and freezing on a NACA0012 airfoil for $\theta = 90$ at different time steps, Re = 50, and Ste = 2

CHAPTER 8 CONCLUSION

In this study, a lattice Boltzmann model for droplets impact and freezing has been described and implemented. We used a double distribution function approach to couple the multi-phase pseudo-potential model and the total enthalpy model for phase change. The coupling has been made through the application of the Immersed Boundary Scheme. The proposed model is finally applied to simulate the freezing of water droplets under different conditions and configurations.

8.1 Summary of Works

First of all, we carried out a literature review where we identified the phenomena involved in the freezing process of water droplets. The limitations of the measurement techniques of this transient process make it difficult for the experimental observation. For that reason, the numerical simulation may provide more details of this complex physical phenomenon. In this context, the lattice Boltzmann method emerges as an alternative to current CFD techniques for simulating multi-phase and phase change problems.

After an introduction of the mesoscopic basis of LBM and the verification of its ability to solve weakly compressible flow equations, we presented a multiphase model. The model was verified with two test cases and it showed the capability to simulate high-density ratio multiphase flows.

The potential of LBM to simulate phase change was subsequently presented. The implementation of the novel total enthalpy model revealed the possibility of simulating phase change by solving the BE and without using an iterative model. Besides, the model avoids keeping unvaried thermal properties for the solid and the liquid.

These two models were coupled to simulate the freezing of water droplets. Qualitative comparison of a three-dimensional model with experimental and simulation results revealed the potential of our model. We observed how the concave interface and volume expansion were properly displayed by the simulation. A 2D model was then used to analyze the influences of some parameters on the static solidification of a droplet on a cold flat plate. The simulation results proved that higher contact angles (corresponding to hydrophobic surfaces) delay the freezing because of the reduced contact area with the surface. Additionally, the Stefan

number (related to the wall temperature) decreases dramatically the total freezing process for higher values (corresponding to cooler temperatures of the wall).

The impact and freezing were later performed. The instant freezing was simulated and we observed how higher impact velocities result in a larger contact area and therefore faster freezing. Finally, the potential of the model for simulating several droplets and freezing on curved surfaces was exhibited by the simulation of water droplets impact and freezing on an airfoil.

8.2 Limitations

Like every model, the assumptions and simplifications made could prevent it from imitating real-life or field conditions. Besides, some undesirable effects may appear. In consequence, the main issues of the proposed models are presented below :

1. The spurious currents are inherent to the pseudo-potential model. These unwanted velocities are introduced into the thermal field through the equilibrium distribution function and it could conduct to a non-physical thermal field.

2. The modeling of gas-liquid flows with a multi-phase model does not allow to change the kinematic viscosity between phases.

3. The activation of the thermal field once the droplet makes contact with the surface is a reasonable hypothesis as it is the surface that provides the nucleation point. However, this does not allow to simulate a droplet which impacts over another frozen droplet, for example.

4. When using the 3D model, the mesh refinement is limited. A large number of degrees of freedom exceeds computational resources.

8.3 Future Research

Even though the field of fluid flow simulations by the lattice Boltzmann method is relatively young, the limitations mentioned before could be solved with some modifications. In the same order, we propose some solutions that could improve the proposed model.

1. The inclusion of the multiple relaxation time for the collision of the velocity field can reduce the spurious currents of the pseudo-potential model.

2. To be able to change viscosity between air and liquid phases, a multi-component model with a double distribution function can be applied.

3. The freezing of droplets over other freezing droplets could be solved by implementing a temperature boundary condition at the interface of droplets.

4. For the limitation of the 3D model, a multi-GPU version of the current code would allow a mesh refinement to improve accuracy.

REFERENCES

[1] U. Ghia, K. Ghia, and C. Shin, "High-re solutions for incompressible flow using the navier-stokes equations and a multigrid method," *Journal of Computational Physics*, vol. 48, no. 3, pp. 387 – 411, 1982.

[2] Y. Peng, Y. Fei Mao, B. Wang, and B. Xie, "Study on c-s and p-r eos in pseudo-potential lattice boltzmann model for two-phase flows," *International Journal of Modern Physics C*, vol. 28, 09 2017.

[3] J. Mencinger, "Numerical simulation of melting in two-dimensional cavity using adaptive grid," *Journal of Computational Physics*, vol. 198, no. 1, pp. 243 – 264, 2004.

[4] H. Zhang, Y. Zhao, R. Lv, and C. Yang, "Freezing of sessile water droplet for various contact angles," *International Journal of Thermal Sciences*, vol. 101, pp. 59 – 67, 2016.

[5] G. Chaudhary and R. Li, "Freezing of water droplets on solid surfaces: An experimental and numerical study," *Experimental Thermal and Fluid Science*, vol. 57, pp. 86 – 93, 2014.

[6] T. P. Ratvasky, B. P. Barnhart, and S. Lee, "Current methods modeling and simulating icing effects on aircraft performance, stability, control," *Journal of Aircraft*, vol. 47, no. 1, pp. 201–211, 2010.

[7] J. Sun, J. Gong, and G. Li, "A lattice boltzmann model for solidification of water droplet on cold flat plate," *International Journal of Refrigeration*, vol. 59, pp. 53 – 64, 2015.

[8] M. Khalili, H. Yahyazadeh, M. Gorji-Bandpy, and D. Ganji, "Application of volume of fluid method for simulation of a droplet impacting a fiber," *Propulsion and Power Research*, vol. 5, no. 2, pp. 123 – 133, 2016.

[9] M. Mohammadi, M. Tembely, and A. Dolatabadi, "Supercooled water droplet impacting superhydrophobic surfaces in the presence of cold air flow," *Applied Sciences*, vol. 7, p. 130, 01 2017.

[10] H. Li, I. V. Roisman, and C. Tropea, "Water drop impact on cold surfaces with solidification," *AIP Conference Proceedings*, vol. 1376, no. 1, pp. 451–453, 2011.

[11] Q. Xu, Z. Li, J. Wang, and R. Wang, "Characteristics of single droplet impact on cold plate surfaces," *Drying Technology*, vol. 30, no. 15, pp. 1756–1762, 2012.

[12] K.-Y. Law, "Definitions for hydrophilicity, hydrophobicity, and superhydrophobicity: Getting the basics right," *The Journal of Physical Chemistry Letters*, vol. 5, no. 4, pp. 686–688, 2014.

[13] L. Huang, Z. Liu, Y. Liu, Y. Gou, and L. Wang, "Effect of contact angle on water droplet freezing process on a cold flat surface," *Experimental Thermal and Fluid Science*, vol. 40, p. 74–80, 07 2012.

[14] Z. Jin, D. Sui, and Z. Yang, "The impact, freezing, and melting processes of a water droplet on an inclined cold surface," *International Journal of Heat and Mass Transfer*, vol. 90, pp. 439–453, 07 2015.

[15] Z. Jin, H. Zhang, and Z. Yang, "Experimental investigation of the impact and freezing processes of a water droplet on an ice surface," *International Journal of Heat and Mass Transfer*, vol. 109, pp. 716 – 724, 2017.

[16] J. Blake, D. Thompson, D. Raps, and T. Strobl, "Simulating the freezing of supercooled water droplets impacting a cooled substrate," *AIAA Journal*, vol. 53, no. 7, pp. 1725–1739, 2015.

[17] Q. Li, K. Luo, Q. Kang, Y. He, Q. Chen, and Q. Liu, "Lattice boltzmann methods for multiphase flow and phase-change heat transfer," *Progress in Energy and Combustion Science*, vol. 52, pp. 62 – 105, 2016.

[18] S. Tabakova and F. Feuillebois, "On the solidification of a supercooled liquid droplet lying on a surface," *Journal of Colloid and Interface Science*, vol. 272, no. 1, pp. 225 – 234, 2004.

[19] M. Tembely, R. Attarzadeh, and A. Dolatabadi, "On the numerical modeling of supercooled micro-droplet impact and freezing on superhydrophobic surfaces," *International Journal of Heat and Mass Transfer*, vol. 127, pp. 193 – 202, 2018.

[20] A. K. Gunstensen, D. H. Rothman, S. Zaleski, and G. Zanetti, "Lattice boltzmann model of immiscible fluids," *Phys. Rev. A*, vol. 43, pp. 4320–4327, Apr 1991.

[21] X. Shan and H. Chen, "Lattice boltzmann model for simulating flows with multiple phases and components," *Physical review. E, Statistical physics, plasmas, fluids, and related interdisciplinary topics*, vol. 47, pp. 1815–1819, 04 1993.

[22] X. He, S. Chen, and R. Zhang, "A lattice boltzmann scheme for incompressible multiphase flow and its application in simulation of rayleigh–taylor instability," *Journal of Computational Physics*, vol. 152, no. 2, pp. 642 – 663, 1999.

[23] M. R. Swift, W. R. Osborn, and J. M. Yeomans, "Lattice boltzmann simulation of nonideal fluids," *Phys. Rev. Lett.*, vol. 75, pp. 830–833, Jul 1995.

[24] R. Huang and H. Wu, "Phase interface effects in the total enthalpy-based lattice boltzmann model for solid–liquid phase change," *Journal of Computational Physics*, vol. 294, pp. 346 – 362, 2015.

[25] W. Miller, S. Succi, and D. Mansutti, "Lattice boltzmann model for anisotropic liquid-solid phase transition," *Phys. Rev. Lett.*, vol. 86, pp. 3578–3581, Apr 2001.

[26] W.-S. Jiaung, J.-R. Ho, and C.-P. Kuo, "Lattice boltzmann method for the heat conduction problem with phase change," *Numerical Heat Transfer Part B - Fundamentals*, vol. 39, 02 2001.

[27] R. Huang and H. Wu, "An immersed boundary-thermal lattice boltzmann method for solid–liquid phase change," *Journal of Computational Physics*, vol. 277, pp. 305 – 319, 2014.

[28] J. Gong, J. Hou, L. Yang, W. Wu, G. Li, and T. Gao, "Mesoscopic investigation of frost crystal nucleation on cold surface based on the lattice-boltzmann method," *Journal of Mechanical Science and Technology*, vol. 33, no. 4, pp. 1925–1935, 2019.

[29] P. Xu, S. Xu, Y. Gao, and P. Liu, "A multicomponent multiphase enthalpy-based lattice boltzmann method for droplet solidification on cold surface with different wettability," *International Journal of Heat and Mass Transfer*, vol. 127, pp. 136 – 140, 2018.

[30] J. Zhao, X. Li, and P. Cheng, "Lattice boltzmann simulation of a droplet impact and freezing on cold surfaces," *International Communications in Heat and Mass Transfer*, vol. 87, 07 2017.

[31] W. Xiong and P. Cheng, "Mesoscale simulation of a molten droplet impacting and solidifying on a cold rough substrate," *International Communications in Heat and Mass Transfer*, vol. 98, pp. 248 – 257, 2018.

[32] T. Krüger, H. Kusumaatmaja, A. Kuzmin, O. Shardt, G. Silva, and E. M. Viggen, *The Lattice Boltzmann Method - Principles and Practice*, 10 2016.

[33] P. L. Bhatnagar, E. P. Gross, and M. Krook, "A model for collision processes in gases. i. small amplitude processes in charged and neutral one-component systems," *Phys. Rev.*, vol. 94, pp. 511–525, May 1954.

[34] S. Succi, *The Lattice Boltzmann Equation for Fluid Dynamics and Beyond*. Oxford: Clarendon Press, 2001.

[35] Q. Zou and X. He, "On pressure and velocity boundary conditions for the lattice boltzmann bgk model," *Physics of Fluids*, vol. 9, no. 6, p. 1591–1598, Jun 1997.

[36] J. R. K. Latt, "Hydrodynamic limit of lattice boltzmann equations," 2007.

[37] P. Yuan and L. Schaefer, "Equations of state in a lattice boltzmann model," *Physics of Fluids*, vol. 18, no. 4, p. 042101, 2006.

[38] D. Zhang, K. Papadikis, and S. Gu, "Investigations on the droplet impact onto a spherical surface with a high density ratio multi-relaxation time lattice-boltzmann model," *Communications in Computational Physics*, vol. 16, no. 4, p. 892–912, 2014.

[39] S. Leclaire, M. El-Hachem, J.-Y. Trépanier, and M. Reggio, "High order spatial generalization of 2d and 3d isotropic discrete gradient operators with fast evaluation on gpus," *Journal of Scientific Computing*, vol. 59, no. 3, pp. 545–573, Jun 2014.

[40] D.-Y. Peng and D. B. Robinson, "A new two-constant equation of state," *Industrial & Engineering Chemistry Fundamentals*, vol. 15, no. 1, pp. 59–64, 1976.

[41] R. C. Reid, J. M. Prausnitz, and T. K. Sherwood, *The properties of gases and liquids*, 3rd ed. McGraw-Hill New York, 1977.

[42] L. Chen, Q. Kang, Y. Mu, Y.-L. He, and W.-Q. Tao, "A critical review of the pseudopotential multiphase lattice boltzmann model: Methods and applications," *International Journal of Heat and Mass Transfer*, vol. 76, pp. 210 – 236, 2014.

[43] S. Gong and P. Cheng, "Numerical investigation of droplet motion and coalescence by an improved lattice boltzmann model for phase transitions and multiphase flows," *Computers Fluids*, vol. 53, pp. 93 – 104, 2012.

[44] A. Kupershtokh, D. Medvedev, and D. Karpov, "On equations of state in a lattice boltzmann method," *Computers Mathematics with Applications*, vol. 58, no. 5, pp. 965 – 974, 2009, mesoscopic Methods in Engineering and Science.

[45] Z. Guo, B. Shi, and C. Zheng, "A coupled lattice bgk model for the boussinesq equations," *International Journal for Numerical Methods in Fluids*, vol. 39, pp. 325 – 342, 06 2002.

[46] C. W. David, "The van der waals equation as a cubic," 2015.

[47] R. Huang, H. Wu, and P. Cheng, "A new lattice boltzmann model for solid–liquid phase change," *International Journal of Heat and Mass Transfer*, vol. 59, pp. 295 – 301, 2013.

[48] D. Li, Z.-X. Tong, Q. Ren, Y.-L. He, and W.-Q. Tao, "Three–dimensional lattice boltzmann models for solid–liquid phase change," *International Journal of Heat and Mass Transfer*, vol. 115, pp. 1334 – 1347, 2017.

[49] D. R. Noble and J. R. Torczynski, "A lattice-boltzmann method for partially saturated computational cells," *International Journal of Modern Physics C*, vol. 09, no. 08, pp. 1189–1201, 1998.

[50] S. Leclaire, K. Abahri, R. Belarbi, and R. Bennacer, "Modeling of static contact angles with curved boundaries using a multiphase lattice boltzmann method with variable density and viscosity ratios," *International Journal for Numerical Methods in Fluids*, vol. 82, no. 8, pp. 451–470, 2016.

[51] M. Yoshino and T. Inamuro, "Lattice boltzmann simulations for flow and heat/mass transfer problems in a three-dimensional porous structure," *International Journal for Numerical Methods in Fluids*, vol. 43, no. 2, pp. 183–198, 2003.

[52] C. Zhang, H. Zhang, W. Fang, Y. Zhao, and C. Yang, "Axisymmetric lattice boltzmann model for simulating the freezing process of a sessile water droplet with volume change," *Phys. Rev. E*, vol. 101, p. 023314, Feb 2020.

APPENDIX A CONTACT ANGLE CALCULATION

The contact angle indicates how a liquid will spread over a surface. It depends on the physical properties of materials as the contact angle represents a manifestation of the molecular interaction between the liquid and the surface. The contact angle allows us to measure the wettability of a surface.

When the liquid and vapour interface meet the solid, there are three forces exerted by the surface tension at three interfaces as shown in Fig. (A.1). The equilibrium of these forces is

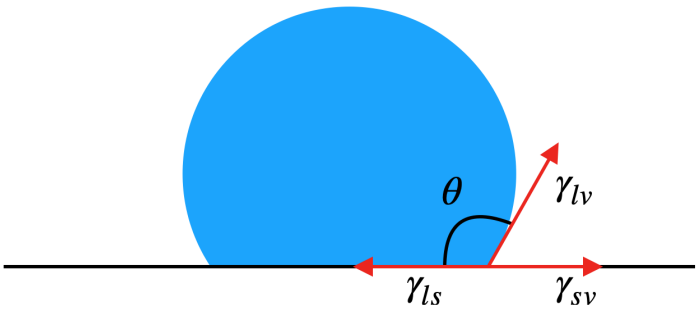

Figure A.1 Contact angle surface tensions : γ_{sv} (at the interface of the solid and vapor phases), γ_{sl} (at the interface of the solid and liquid phases), and γ_{lv} (at the interface of the liquid and vapor phases).

determined via Young's equation which makes appear the contact angle :

$$\gamma_{sv} = \gamma_{ls} + \gamma_{lv}\cos\theta \tag{A.1}$$

However, in practice we calculate the contact angle through the shape of the equilibrium droplet over a surface. There are some alternatives that can be used. We will use the one that assumes that the droplet is a sphere. When the baseline (horizontal line that represents the solid) and the trace of the droplet edge are determined, the contact angle can be calculated by measuring the width (b) and the height (h) of the droplet as shown in Fig. (A.2). First, the parameter r is calculated :

$$r = \frac{4h^2 + b^2}{8h} \tag{A.2}$$

The contact angle θ is then calculated as :

$$\theta^* = \text{atan}\left(\frac{b}{2(r-h)}\right) \tag{A.3}$$

$$\theta = \begin{cases} \theta^* & \theta^* > 0 \\ \theta^* + 180^\circ & \theta^* < 0 \end{cases} \tag{A.4}$$

If $\theta = 0°$ there is a complete wetting. When $0° < \theta < 90°$ the surface is considered hydrophilic (the solid is wettable) and for $\theta > 90°$ the surface is considered hydrophobic (the solid is not wettable).

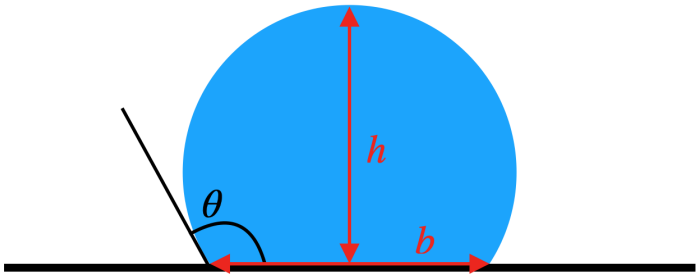

Figure A.2 Geometry of contact angle measurement.

APPENDIX B 3D MODEL

The implementation of a three-dimensional model uses a different stencil for the discrete velocities of the LBM and in consequence a different weighted coefficients.

A D3Q19 stencil as shown in Fig. (B.1) was used and the weighted coefficients are given by :

$$\omega_i = \begin{cases} 1/3 & i = 0 \\ 1/18 & i = 1, 2, 3, 10, 11, 12 \\ 1/36 & i = 4, 5, 6, 7, 8, 9, 13, 14, 15, 16, 17, 18 \end{cases} \tag{B.1}$$

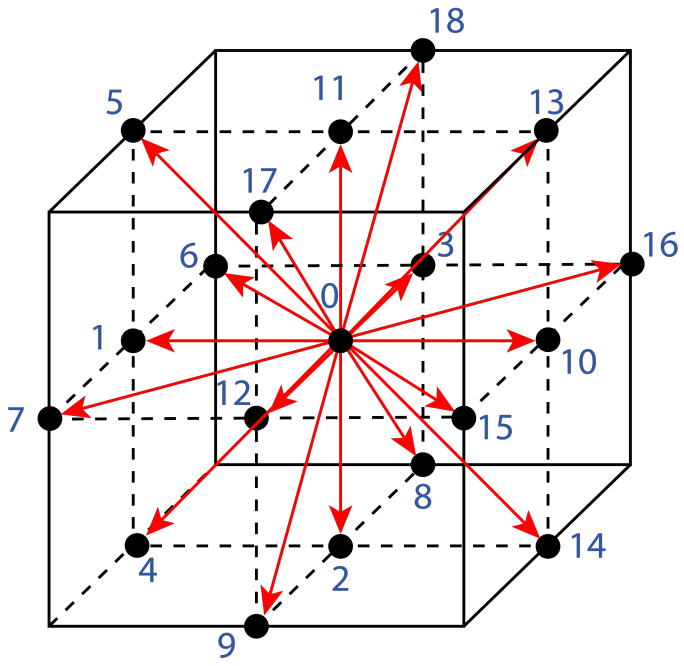

Figure B.1 D3Q19 stencil.